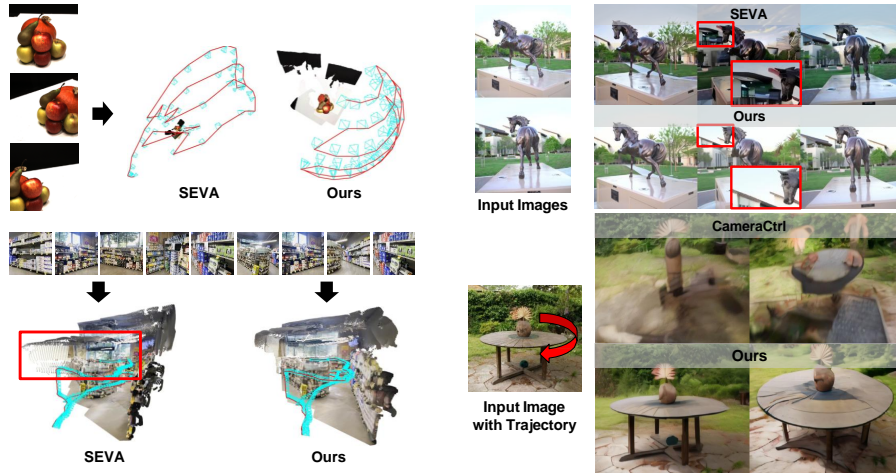


# GeoNVS: Geometry Grounded Video Diffusion for Novel View Synthesis

Minjun Kang<sup>1</sup>, Inkyu Shin<sup>2</sup>, Taeyeop Lee<sup>1</sup>, Myungchul Kim<sup>1</sup>,  
In So Kweon<sup>1</sup>, and Kuk-Jin Yoon<sup>1</sup>

<sup>1</sup>KAIST, South Korea <sup>2</sup>Luma AI, USA



**Fig. 1** We demonstrate **GeoNVS**, integrated into SEVA [90] and CameraCtrl [24], consistently enhancing geometric fidelity and camera controllability, while resolving photometric inconsistencies (**right-top**) across challenging large-scale indoor and outdoor scenes. Our approach consistently outperforms existing methods. [Project page](#).

**Abstract.** Novel view synthesis requires strong 3D geometric consistency and the ability to generate visually coherent images across diverse viewpoints. While recent camera-controlled video diffusion models show promising results, they often suffer from geometric distortions and limited camera controllability. To overcome these challenges, we introduce **GeoNVS**, a geometry-grounded novel-view synthesizer that enhances both geometric fidelity and camera controllability through explicit 3D geometric guidance. Our key innovation is the Gaussian Splat Feature Adapter (GS-Adapter), which lifts input-view diffusion features into 3D Gaussian representations, renders geometry-constrained novel-view features, and adaptively fuses them with diffusion features to correct geometrically inconsistent representations. Unlike prior methods that inject geometry at the input level, GS-Adapter operates in feature space, avoiding view-dependent color noise that degrades structural consistency. Its plug-and-play design enables zero-shot compatibility with diverse feed-forward geometry models without additional training, and can be adapted to other video diffusion backbones. Experiments across 9 scenes and 18 settings demonstrate state-of-the-art performance, achieving 11.3% and 14.9% improvements over SEVA and CameraCtrl, with up to 2× reduction in translation error and 7× in Chamfer Distance.

## 1 Introduction

Novel View Synthesis (NVS) aims to synthesize photorealistic images from novel viewpoints while preserving the geometric coherence of the observed scene. Neural Radiance Fields (NeRF) [52] and 3D Gaussian Splatting (3D-GS) [35] are representative per-scene optimization solutions that require a large number of observations for training. These methods struggle with sparse-view inputs and are limited to novel views near input viewpoints. Recently, feed-forward geometry methods [7, 10, 44, 63, 65, 70, 80] and generative approaches [19, 24, 25, 71, 89, 90] have emerged as strong alternatives for such challenging scenarios.

**Feed-forward geometry** methods directly estimate explicit 3D representations from sparse-view input images in a single forward pass. One line of work [10, 44, 63, 80] predicts 3D Gaussians directly from inputs and renders novel views via Gaussian splatting. Another line of work [34, 65, 70] first estimates point cloud maps and then requires optimization to fit 3D Gaussians [17]. Despite their strong structural consistency in observed regions, these methods often fail to preserve fine-grained appearance details in low-overlap scenes.

**Generative novel-view synthesis** represents another powerful paradigm for handling sparse-view inputs, enabling dense and semantically rich scene synthesis. These methods incorporate camera [1, 4, 19, 24, 71, 90] or point trajectories [20, 78, 83] into video diffusion models to guide novel view generation. They exhibit remarkable capability even for scenes with low-overlap inputs, overcoming limitations of feed-forward geometry methods. However, these approaches still suffer from multi-view inconsistency, hallucinating structures that deviate from the input images, and limited camera controllability, failing to follow the intended camera trajectories as shown in Fig. 1. A natural remedy is to incorporate explicit geometry priors from feed-forward geometry models to enforce structural consistency between generated and input views.

Indeed, several studies [6, 11, 48, 58, 74–76, 85] have explored this direction, combining geometry priors with generative models to achieve geometrically consistent and dense novel-view synthesis. These methods feed noisy rendered novel-view images [48, 58, 74, 76, 85] or features [6, 11, 75] into a diffusion model for refinement. However, we observe that these input-level fusion methods in Fig. 2-(b) introduce geometric distortions and hallucinated structures in the final output, as noisy textures in the rendered images obscure structural information.

To overcome this limitation, we propose **GeoNVS**, which couples geometry priors with the diffusion model in feature space, enabling the diffusion model to leverage explicit 3D structural information during the denoising process. Our core component, the Gaussian Splatting Feature Adapter (**GS-Adapter**), bridges 3D Gaussians and the diffusion model through a feature embedding and rendering process, modulating geometrically inconsistent diffusion features. Specifically, GS-Adapter (1) embeds 2D input-view diffusion features into 3D Gaussians, (2) rasterizes geometry-aware novel-view features via Gaussian splatting, and (3) adaptively fuses them with novel-view diffusion features to produce geometrically corrected features. By anchoring diffusion features to explicit 3D structure, GS-Adapter ensures that generated pixels are geometrically aligned with the target camera viewpoint, leading to improved camera controllability.

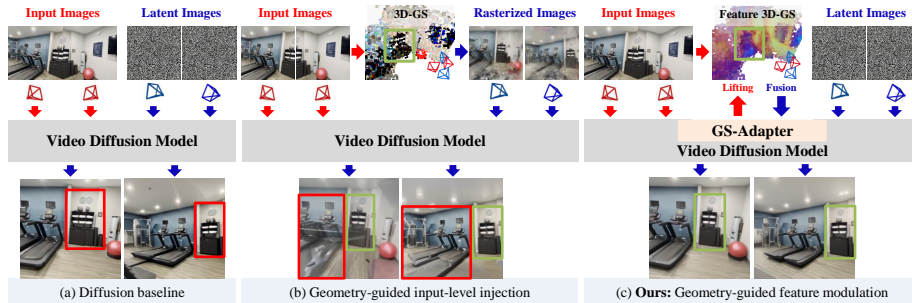


**Fig. 2 Geometry-guided generative NVS.** (a) Pure diffusion model produces view-inconsistent results. Given sparse **input-view** images, both (b) and (c) reconstruct 3D Gaussians from input views using a geometry prior. (b) Previous methods inject rasterized **novel-view** images from 3D-GS as input, causing artifacts from noisy rasterized colors. (c) Our method modulates internal diffusion features via a GS-Adapter conditioned on 3D-GS, achieving superior geometry consistency and visual quality.

Compared to previous methods that perform input-level fusion in Fig. 2-(b), our approach in Fig. 2-(c) leverages only the structural information encoded in 3D Gaussians, avoiding reliance on noisy view-dependent color information. Our modular design enables *plug-and-play* integration with diverse feed-forward geometry models without additional training, while existing methods [11, 40, 73, 85] depend on a specific geometry model, requiring retraining upon substitution. To validate the effectiveness of **GeoNVS**, we integrate GS-Adapter into SEVA [90] and CameraCtrl [24] and evaluate across indoor and outdoor scenes in both low- and large-overlap settings as well as long-trajectory generation, demonstrating consistent improvements in geometric consistency, camera controllability, and photorealistic quality. In summary, our key contributions are as follows:

- We propose **GS-Adapter**, which couples 3D Gaussian priors with the diffusion model in feature space, improving geometric consistency and camera controllability in video diffusion-based novel-view synthesis.
- Our modular design supports diverse combinations of feed-forward geometry models and video diffusion backbones without additional training, enabling flexible plug-and-play applicability.
- **GeoNVS** achieves state-of-the-art performance over existing generative NVS methods across diverse indoor and outdoor benchmarks, evaluated on 9 scenes and 18 settings.

## 2 Related Work

**Sparse-view Novel View Synthesis.** NeRF [52] and 3D-GS [35] achieve photorealistic novel-view synthesis given dense inputs, but overfit severely under sparse views. To resolve this, prior works introduce depth supervision [12, 13, 64, 93] or normal consistency [62, 87], yet remain sensitive to constraint quality. Feed-forward geometry methods [7, 10, 63, 80] directly predict 3D Gaussians using cost volumes [14, 21, 29, 82] or monocular depth [15, 81, 84], and geometry foundation models [34, 44, 65, 70] further enhance reconstruction quality at scale. We leverage these priors to guide the diffusion model toward structural consistency.

**Generative Novel View Synthesis.** Diffusion models have evolved into powerful task executors by incorporating controllable conditioning signals [41, 88]. Camera-controlled video diffusion methods embed camera poses [71], Plücker coordinates [1, 4, 19, 24, 25, 90], trajectory-based attention [89], or projected 3D point maps [22] to guide video generation. Recently, SEVA [90] demonstrated strong novel-view synthesis via a multi-view diffusion model trained on large-scale datasets. Building on SEVA and CameraCtrl, we enhance these baselines to achieve geometrically consistent generation and improved controllability.

**Feature field distillation for 3D-GS.** Beyond radiance fields, embedding semantic features into 3D representations [36, 54] has enabled various downstream applications [28, 31, 39, 43, 67]. Most existing methods [42, 54, 91] distill semantic features [5, 37, 53, 55] into 3D Gaussians via per-scene optimization. Recently, Dr.Splat [33] introduced feed-forward feature distillation into 3D Gaussians, enabling fast 3D localization without per-scene optimization. LUDVIG [49] extends this to integrate DINOv2 [53] features into 3D scene geometry through graph diffusion for semantic segmentation. Unlike prior methods that distill static semantic features, diffusion features vary across denoising timesteps, making per-scene optimization infeasible. We therefore adopt a direct feed-forward lifting approach, extending it to preserve pixel-level feature fidelity rather than coarse instance-level distinctions sufficient for segmentation.

### 3 Method

In this section, we first provide preliminaries on the problem formulation, geometry prior construction, and Gaussian splatting background in Sec. 3.1. We then introduce **GS-Adapter** in Sec. 3.2, our core module that leverages 3D Gaussian priors to correct geometrically inconsistent diffusion features, thereby enforcing geometric consistency and improving camera controllability. Finally, we describe the integration of GS-Adapter into an existing video diffusion framework via multi-scale feature aggregation in Sec. 3.3.

#### 3.1 Preliminary

**Problem Formulation.** Given  $P$  reference images  $\mathbf{I}_{\text{ref}} \in \mathbb{R}^{P \times hw \times 3}$  and their corresponding camera poses  $\boldsymbol{\pi}^{\text{ref}}$ , the NVS task is to synthesize  $Q$  target views  $\mathbf{I}_{\text{tgt}} \in \mathbb{R}^{Q \times hw \times 3}$  for the target camera poses  $\boldsymbol{\pi}^{\text{tgt}}$ . **GeoNVS** supports an arbitrary number of reference images, as both SEVA [90] and the geometry models natively handle monocular and multi-view inputs.

**Geometry Prior.** Our method requires 3D Gaussians  $\mathcal{G}$  as structural guidance for the diffusion model. We utilize feed-forward geometry models [10, 63, 65, 70, 80] to estimate this geometry prior from the reference images. For geometry models that estimate both camera poses and point clouds (VGGT [65] and Pi3 [70]), we align the predicted camera scale  $s^*$  to the target cameras by solving:

$$s^* = \arg \min_s \|\mathbf{C}^{\text{gt}} - s \mathbf{C}^{\text{pred}}\|_2^2 \quad (1)$$

where  $\mathbf{C}^{\text{gt}}$  and  $\mathbf{C}^{\text{pred}}$  denote the target and predicted camera centers, respectively. We then fit 3D Gaussians initialized from the estimated point clouds [17].

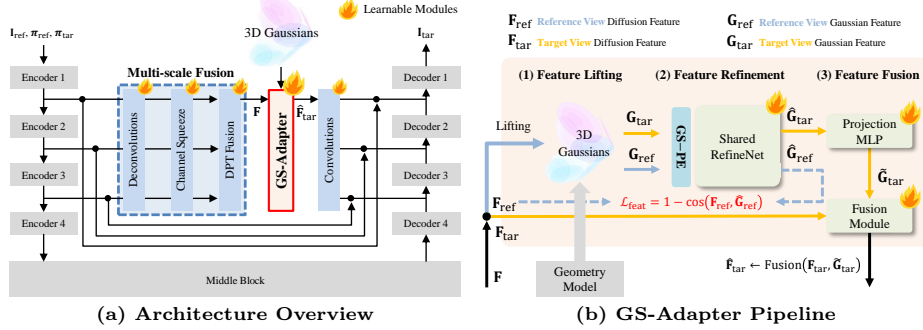


**Fig. 3 GeoNVS architecture.** (a) Overview of the integration with a video diffusion model. (b) The GS-Adapter pipeline for feature lifting, refinement, and fusion. All learnable modules (🔥) are trained with LoRA [26]. During training, a consistency loss  $\mathcal{L}_{\text{feat}}$  is applied to preserve geometric detail lost during feature lifting. Please refer to the supplementary material for details of the multi-scale fusion module and RefineNet.

**3D Gaussian Splatting.** 3D Gaussian Splatting [35] represents a scene with  $N$  Gaussian particles composed of position  $\boldsymbol{\mu} \in \mathbb{R}^3$ , rotation  $\boldsymbol{r} \in \mathbb{R}^4$  via quaternions, scale  $\boldsymbol{s} \in \mathbb{R}^3$ , opacity  $\boldsymbol{\sigma} \in \mathbb{R}^1$ , and color represented by spherical harmonics. The color at pixel  $p$  for view  $d$  is obtained by summing contributions of Gaussians:

$$C(d, p) = \sum_{i=1}^N c_i(d) w_i(d, p), \quad w_i(d, p) = \alpha_i(d, p) \prod_{j=1}^{i-1} (1 - \alpha_j(d, p)) \quad (2)$$

where  $\alpha_i(d, p)$  is the product of the opacity  $\sigma_i$  and the 2D projected Gaussian density  $\mathcal{N}_i$  at pixel position  $p$ . Similarly, feature rasterization is represented as:

$$\mathbf{F}(d, p) = \sum_{i=1}^N \mathbf{f}_i w_i(d, p) \quad (3)$$

### 3.2 GS-Adapter: Geometry-Guided Diffusion Feature Adaptation

Given the diffusion features  $\mathbf{F}^t$  at denoising timestep  $t$  and 3D Gaussians prior  $\mathcal{G}$ , GS-Adapter is designed to obtain geometry-augmented features  $\hat{\mathbf{F}}^t$ , formulated as  $\hat{\mathbf{F}}^t = \Phi(\mathbf{F}^t, \mathcal{G})$ . Diffusion features  $\mathbf{F}^t = [\mathbf{F}_{\text{ref}}^t; \mathbf{F}_{\text{tar}}^t]$  consist of reference-view (input-view) features  $\mathbf{F}_{\text{ref}}^t \in \mathbb{R}^{P \times \frac{h}{n} \times \frac{w}{n} \times C}$  and novel-view features  $\mathbf{F}_{\text{tar}}^t \in \mathbb{R}^{Q \times \frac{h}{n} \times \frac{w}{n} \times C}$ , where  $n$  denotes the downsampling factor of the Variational Autoencoder (VAE), and  $C$  denotes the channel dimension of the diffusion features. For convenience, we omit the superscript  $t$  hereafter. As illustrated in Fig. 3(b), GS-Adapter consists of three major steps: (1) **feature lifting**: projecting reference-view diffusion features onto 3D Gaussians, (2) **feature refinement**: refining the rendered novel-view features to recover fine-grained details, and (3) **feature fusion**: combining the geometry-guided features with the original diffusion features to obtain the revised diffusion features.

**Uplifting diffusion feature into 3D-GS.** Since the diffusion features vary across timesteps and our method requires obtaining geometry-augmented features at every denoising timestep, per-scene optimization-based feature embedding approaches [42, 54, 91] are not feasible, as they cannot adapt to the contin-

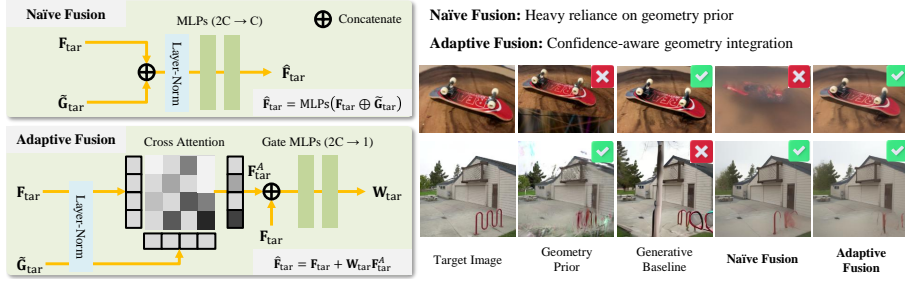


**Fig. 4 Feature fusion module of GS-Adapter.** Two fusion approaches are proposed to integrate the diffusion feature  $\mathbf{F}_{\text{tar}}$  and the geometry-aware feature  $\hat{\mathbf{G}}_{\text{tar}}$ , producing the updated novel-view feature  $\hat{\mathbf{F}}_{\text{tar}}$ . We adopt adaptive fusion as it remains effective even when either the geometry prior or the generative model fails.

uously changing feature distribution during denoising. Inspired by [33, 49], we obtain uplifted diffusion features for each Gaussian as a weighted average of 2D reference diffusion features  $\mathbf{F}_{\text{ref}}$ . Each 2D feature at the viewing direction  $d$  and pixel  $p$  contributes to the Gaussian feature  $\mathbf{f}_i$  proportionally to the rendering weight  $w_i(d, p)$  with normalization, where  $\mathcal{I}_i$  denotes the set of view/pixel pairs contributing to each Gaussian. The uplifted feature  $\hat{\mathbf{f}}_i \in \mathbb{R}^C$  is defined as:

$$\hat{\mathbf{f}}_i = \frac{\mathbf{f}_i}{\|\mathbf{f}_i\|_2}, \quad \mathbf{f}_i = \sum_{(d,p) \in \mathcal{I}_i} \frac{w_i(d,p)}{\sum_{(d',p') \in \mathcal{I}_i} w_i(d',p')} \mathbf{F}_{\text{ref}}(d,p) \quad (4)$$

This feed-forward uplifting enables explicit participation of 3D Gaussians at every denoising step, allowing end-to-end training with the diffusion model.

**Feature refinement.** After uplifting  $\mathbf{F}_{\text{ref}}$  into the 3D Gaussians, we rasterize the geometry-constrained novel-view features  $\mathbf{G}_{\text{tar}} \in \mathbb{R}^{Q \times \frac{h}{n} \times \frac{w}{n} \times C}$  using Eq. (3). Our next goal is to fuse these geometry-aware features with the original novel-view diffusion features  $\mathbf{F}_{\text{tar}}$ . However, we observe that direct fusion alone is insufficient for recovering fine-grained details, as shown in Fig. 5, consistent with the findings of [49]. To compensate for the information loss during lifting and rendering, we augment the rendered features  $\mathbf{G}$  with Gaussian positional encoding (GS-PE) and refine them using a lightweight ResNet-based refinement network,  $\mathcal{R}$ . Specifically, for each pixel  $(d, p)$ , we identify the most contributing Gaussian  $i^*(d, p) = \arg \max_i w_i(d, p)$ , normalize its 3D center within the scene bounding box, and encode it alongside the rendering weight  $w^*(d, p)$  via sinusoidal encoding  $\gamma(\cdot)$  to obtain the positionally-encoded features  $\mathbf{G}'$ :

$$\mathbf{G}'(d, p) = \mathbf{G}(d, p) + [\gamma(\tilde{x}) \parallel \gamma(\tilde{y}) \parallel \gamma(\tilde{z}) \parallel \gamma(w^*)] \quad (5)$$

where  $\tilde{\mathbf{x}}(d, p) = (\tilde{x}, \tilde{y}, \tilde{z})$  denotes the normalized 3D center of  $i^*(d, p)$ , and  $\gamma(v) = [\sin(\omega_k v), \cos(\omega_k v)]_{k=0}^{D'/2-1}$  with  $\omega_k = \omega_0^{-2k/D'}$  and  $D' = C/4$ . This equips the refinement network with explicit 3D structural cues. Afterwards, we get refined features  $\hat{\mathbf{G}} = \mathcal{R}(\mathbf{G}')$ . Because the original input-view features  $\mathbf{F}_{\text{ref}}$  serve as a reliable reference, we supervise  $\mathcal{R}$  by aligning the refined input-view features  $\hat{\mathbf{G}}_{\text{ref}} \in \mathbb{R}^{P \times \frac{h}{n} \times \frac{w}{n} \times C}$  with  $\mathbf{F}_{\text{ref}}$  during training via a cosine similarity loss:

$$\mathcal{L}_{\text{feat}} = \left\| 1 - \frac{\hat{\mathbf{G}}_{\text{ref}} \cdot \mathbf{F}_{\text{ref}}}{\|\hat{\mathbf{G}}_{\text{ref}}\|_2 \|\mathbf{F}_{\text{ref}}\|_2} \right\|_2 \quad (6)$$

**Adaptive feature fusion.** Given the refined novel-view features  $\tilde{\mathbf{G}}_{\text{tar}} = \mathcal{P}(\hat{\mathbf{G}}_{\text{tar}})$ , where  $\mathcal{P}$  denotes an MLP projection, we fuse them with the original diffusion features  $\mathbf{F}_{\text{tar}}$  to obtain the geometry-augmented features  $\hat{\mathbf{F}}_{\text{tar}}$ . To this end, we explore two fusion approaches: Naïve Fusion and Adaptive Fusion in Fig. 4. A naïve approach is to directly concatenate  $\mathbf{F}_{\text{tar}}$  and  $\tilde{\mathbf{G}}_{\text{tar}}$  and project them back to the original channel dimension via an MLPs:

$$\hat{\mathbf{F}}_{\text{tar}} = \text{MLPs}(\mathbf{F}_{\text{tar}} \oplus \tilde{\mathbf{G}}_{\text{tar}}) \quad (7)$$

However, as shown in Fig. 4, naïve fusion heavily relies on the geometry prior quality and fails when the prior is corrupted. To address this, we propose an **adaptive fusion** that selectively incorporates geometric information based on its local reliability. Specifically, we first apply cross-attention with  $\mathbf{F}_{\text{tar}}$  as query and  $\tilde{\mathbf{G}}_{\text{tar}}$  as key and value to obtain geometry-attended features  $\mathbf{F}_{\text{tar}}^A$ . We then predict a pixel-wise confidence weight  $\mathbf{W}_{\text{tar}} \in [-1, 1]$  via a gating MLP conditioned on both  $\mathbf{F}_{\text{tar}}$  and  $\mathbf{F}_{\text{tar}}^A$  and get  $\hat{\mathbf{F}}_{\text{tar}}$  by weighted sum of  $\mathbf{F}_{\text{tar}}$  and  $\mathbf{F}_{\text{tar}}^A$ :

$$\mathbf{F}_{\text{tar}}^A = \text{CrossAttn}(\mathbf{F}_{\text{tar}}, \tilde{\mathbf{G}}_{\text{tar}}), \quad \mathbf{W}_{\text{tar}} = \text{Tanh}(\text{MLP}(\mathbf{F}_{\text{tar}} \oplus \mathbf{F}_{\text{tar}}^A)) \quad (8)$$

$$\hat{\mathbf{F}}_{\text{tar}} = \mathbf{F}_{\text{tar}} + \mathbf{W}_{\text{tar}} \cdot \mathbf{F}_{\text{tar}}^A \quad (9)$$

The residual formulation preserves the original diffusion features when geometric guidance is unreliable, while the Tanh activation allows both positive and negative corrections, as illustrated in Fig. 4.

### 3.3 Integration into Video Diffusion

**Integrating 3D-GS into video diffusion.** GeoNVS incorporates explicit 3D structural information into the denoising process by coupling 3D Gaussians with the diffusion model in feature space. At each denoising timestep  $t$ , GS-Adapter embeds  $\mathbf{F}_{\text{ref}}^t$  into 3D Gaussians, rasterizes geometry-aware novel-view features, and adaptively injects them back into the diffusion model to correct geometrically inconsistent features throughout the entire denoising process.

**Multi-scale feature aggregation.** Multi-scale features play a crucial role in visual understanding [9, 45, 56, 66, 69] and generation [47, 59]. To effectively combine geometry-guided features with diffusion features across different spatial scales, we leverage multi-scale encoder features via a DPT-style [56] aggregation strategy, upsampling and hierarchically merging them to a unified feature of  $\mathbf{F} \in \mathbb{R}^{(P+Q) \times \frac{h}{n} \times \frac{w}{n} \times C}$  before feeding into GS-Adapter (see Fig. 3). The geometry-corrected features are then downsampled to the original resolutions and added through skip connections to the decoder. We validate this design in Sec. 4.6.

**Loss function.** We train the multi-scale fusion module and GS-Adapter alongside trainable LoRA [26] layers injected into the attention modules of the frozen video diffusion model. The total training objective is formulated by combining the latent space alignment loss [3] and the feature alignment loss from Eq. (6):

$$\mathcal{L} = \mathcal{L}_{\text{latent}} + 0.05\mathcal{L}_{\text{feat}} \quad (10)$$

## 4 Experiment

### 4.1 Overview

We organize our experiments to validate three key claims of GeoNVS. First, GS-Adapter improves geometric consistency and camera controllability, quantified by camera pose error and Chamfer Distance, and further supported by a feature consistency metric (Secs. 4.4 and 4.5). Second, GeoNVS achieves state-of-the-art photorealistic quality across diverse scenes, evaluated in Sec. 4.3 on 9 scenes under small/large-viewpoint and long-trajectory settings. Third, GS-Adapter supports plug-and-play integration with diverse geometry models without additional training, and is compatible with other diffusion backbones; we further show that its computational overhead can be substantially reduced via voxel-based Gaussian pruning with negligible performance degradation (Sec. 4.6).

### 4.2 Implementation Details

We implement GeoNVS on two baselines, SEVA [90] and CameraCtrl [24], to demonstrate its compatibility. While the SEVA-based GeoNVS supports an arbitrary number of input and output views, the CameraCtrl-based GeoNVS is limited to a single reference view due to constraints of the baseline model.

**Training setup.** We use the DL3DV-10K [46] dataset to train GeoNVS. Using VGGT [65] and InstantSplat [17], we construct 3D Gaussians paired with 150K clips with varying reference-to-novel view splits  $(P, Q) \in \{(1, 20), (3, 18), (6, 15), (9, 12), (12, 9)\}$  where the total number of views is fixed at 21. Please refer to the supplementary material for details on dataset preprocessing. Both SEVA- and CameraCtrl-based GeoNVS are trained at resolutions  $(h, w)$  of  $384 \times 384$  and  $320 \times 576$  with initial learning rates of  $3 \times 10^{-5}$  and  $1 \times 10^{-4}$ , respectively. Our model is fine-tuned using LoRA [26] on 8 NVIDIA A6000 GPUs (48GB). We set the rank and  $\alpha$  to 16 for SEVA, and 4 for CameraCtrl. The training process takes approximately 80 hours with a total batch size of 8.

**Inference setup.** We evaluate our method on the SEVA benchmark [90], consisting of 9 scenes [2, 30, 38, 46, 51, 57, 77, 79, 92] with input views  $P$  varying from 1 to 9. We include Tanks and Temples [38] under the CF-3DGS sampling protocol [18] for the view interpolation task (T&T O split). For fair comparison, all combined methods (generative + geometry prior) use the same best-performing geometry prior per dataset. Note that MVSplat360 [11] is limited to MVSplat [10] by design. We evaluate all methods on a single A6000 GPU. Please refer to the supplementary material for details, including evaluation dataset splits.

**Input-level injection of geometry prior.** As a baseline for input-level geometry conditioning into the diffusion model in Fig. 2-(b), we implement an input-level injection approach following prior work [50, 74, 76]. Given the VAE-encoded latents  $\mathbf{z}_{\text{tar}}$  of 3D-GS rendered novel-view images, we initialize the noisy latents as  $\mathbf{x}_{\text{tar}} \leftarrow \mathbf{x} \cdot \sigma_{t_0} + \mathbf{z}_{\text{tar}}$ , where  $\sigma_{t_0}$  is the noise scale at the start timestep  $t_0 = \lfloor T \cdot s \rfloor$  determined by a strength  $s \in [0, 1]$ . A larger  $s$  allows the diffusion model more freedom to deviate from the geometry prior, while a smaller  $s$  enforces stronger adherence to the rendered geometry; we set  $s = 0.2$ . We compare this approach against our GS-Adapter, which modulates internal diffusion features with a geometry prior rather than relying on rasterized images.

**Table 1 PSNR  $\uparrow$  on small-viewpoint set NVS.** The small-viewpoint set contains scenes with high view overlap between reference and target views.  $P$  denotes the number of reference images. For  $P=1$ , we sweep the unit length for camera normalization following [90] to resolve scale ambiguity. All combined methods (generative + geometry) use the best feed-forward geometry model per dataset as the geometry prior.

Method	dataset	OO3D [77]					RE10K [92]					LLFF [51]		DTU [30]		CO3D [57]		WRGBD [79]		Mip360 [2]	DL3DV [46]			T&T [38]			Average
	split	S	D	P	R	R	R	R	R	V	R	S <sub>c</sub>	S <sub>a</sub>	R	S	L	O	O	O								
	$P$	3	1	2	1	3	1	3	1	3	1	3	3	6	6	6	9	2	3								
<b>Feed-forward geometry models</b>																											
MVSplat [10]	21.82	10.68	25.56	11.26	23.35	5.69	13.68	7.47	11.35	10.12	12.04	12.89	12.38	13.45	13.89	14.07	12.52	13.45	13.65								
HiSplat [63]	21.98	12.38	25.50	13.89	25.81	5.75	15.16	7.11	12.37	10.59	12.55	13.49	12.48	13.90	14.04	14.20	12.38	15.57	14.40								
DepthSplat [80]	22.66	13.02	25.57	14.49	26.99	5.91	15.02	8.79	14.19	11.29	15.08	13.92	13.50	15.04	15.87	16.88	15.76	17.99	15.67								
VGGT [65]	22.12	13.73	23.98	13.95	27.48	10.89	20.08	7.05	17.15	10.48	15.39	11.09	12.56	15.49	17.09	18.31	20.92	23.96	16.76								
P3 [70]	18.48	10.56	24.35	11.00	27.66	8.80	15.54	8.82	7.81	12.08	12.60	10.54	10.46	13.16	16.03	17.23	14.46	16.98	14.25								
<b>Generative models</b>																											
MotionCtrl [71]	-	13.10	-	13.86	-	11.40	-	8.41	-	13.64	-	-	-	-	-	-	-	-	12.08								
CameraCtrl [24]	-	13.08	-	14.09	-	11.88	-	8.72	-	13.70	-	-	-	-	-	-	-	-	12.29								
ViewCrafter [86]	18.56	14.37	-	17.44	15.83	11.79	11.39	9.22	8.49	15.87	9.89	9.23	9.37	10.81	10.51	9.75	10.74	11.13	12.02								
SEVA [90]	26.28	14.51	22.77	15.25	24.44	12.22	17.12	10.54	17.03	16.29	17.22	15.96	15.71	15.38	15.84	16.87	16.35	18.85	17.15								
<b>Generative model + Geometry prior</b>																											
MVSplat360 [11]	21.45	13.68	20.20	13.44	20.97	12.79	15.31	9.10	11.38	12.69	14.29	14.34	13.22	14.15	15.09	15.26	14.22	15.84	14.86								
GenFusion [76]	20.90	14.87	22.48	15.88	22.69	11.39	17.87	8.36	13.75	12.15	12.99	13.38	12.47	11.99	13.11	14.78	18.25	20.14	15.30								
Difix3D [74]	23.05	12.92	25.23	14.37	27.14	10.85	19.59	8.79	17.22	11.93	15.23	12.60	12.67	14.95	16.33	17.33	20.68	23.36	16.89								
GeoNVS (Ours)	26.58	16.66	24.78	17.62	27.11	14.10	18.29	12.12	19.18	17.14	19.26	18.23	17.12	16.57	18.11	19.66	18.76	22.24	19.09								

### 4.3 Synthesis Quality

**Metrics.** We evaluate synthesis quality using PSNR, SSIM, and LPIPS — standard metrics in NVS — and report PSNR as the primary metric in the main manuscript; full results are in the supplementary material.

**Robustness to viewpoint overlap.** Following SEVA [90], we evaluate on Set NVS, which generates a set of target views in arbitrary order, decomposed into small- and large-viewpoint settings based on the CLIP [55] distance between reference and target views (threshold: 0.11). As shown in Tabs. 1 and 2a and Figs. 6 and 7, our method consistently outperforms comparison methods across most datasets, improving over our baseline SEVA [90] on all benchmarks and demonstrating robustness to both small and large viewpoint changes.

**Long trajectory generation.** Trajectory NVS organizes target views as a smooth camera trajectory forming a video sequence. Leveraging the geometry prior from reference views, we adopt the two-pass sampling method from SEVA [90] to generate consistent, non-flickering long-term videos. As shown in Tabs. 3a and 3b, our method consistently improves over baseline SEVA by a large margin, with performance scaling favorably with more reference views.

### 4.4 Geometric Consistency and Camera Controllability

**Metrics.** To validate geometric fidelity, we reconstruct point clouds and estimate camera trajectories from generated videos using ViPE [27]. Camera controllability is evaluated by the translation error  $T_{err}$ [cm] and rotation error  $R_{err}$ [deg] between estimated and ground-truth camera poses following [24]. Geometric consistency is quantified by mean Chamfer Distance ( $CD$ ) between point clouds reconstructed from generated and ground-truth videos [6, 16]. We exclude scenes where ViPE [27] fails to reconstruct the ground-truth video ( $T_{err}$  or  $R_{err} > 50$ ).

**Table 2 Large-viewpoint set NVS.** The large-viewpoint set contains scenes with low overlap between reference and target views.  $P$  denotes the number of reference images. We use DepthSplat [80] as the geometry prior for both combined methods.

**(a) PSNR  $\uparrow$  results.**

Method	dataset CO3D [57]		WRGBD [79]			Mip360 [2]		DL3DV [46]		Average
	split	R	S <sub>h</sub>		R		S			
			P	1	1	3	1	3	1	
<b>Geometry prior</b>										
DepthSplat [80]		8.54	7.31	11.94	9.20	14.22	7.37	14.67	10.46	
<b>Generative models</b>										
MotionCtrl [71]		11.77	10.33	-	11.04	-	10.99	-	11.03	
CameraCtrl [24]		11.71	10.38	-	10.94	-	11.05	-	11.02	
ViewCrafter [86]		11.11	-	9.32	10.79	10.38	11.18	10.20	10.50	
SEVA [90]		12.27	11.27	13.72	11.19	14.30	11.48	14.27	12.64	
<b>Generative model + Geometry prior</b>										
GenFusion [76]		10.21	9.60	11.37	9.84	11.88	10.11	13.33	10.91	
Difix3D [74]		8.56	7.33	11.81	9.30	13.83	7.48	14.24	10.36	
GeoNVS (Ours)		14.66	12.72	15.08	12.34	15.47	13.07	16.09	14.20	

**Table 3 Long trajectory NVS.** The long trajectory NVS is to measure the long-term generation ability of generative NVS.  $P$  denotes the number of reference images. We use VGGT [65] as the geometry prior for our method.

**(a) PSNR  $\uparrow$  results.**

Method	dataset $P$	Mip360 [2]			DL3DV [46]			T&T [38]		
		3	6	9	3	6	9	2	3	6
		DepthSplat [80]	13.22	13.91	14.57	14.79	15.90	16.68	15.69	17.51
VGGT [65]	12.16	14.45	15.80	15.43	16.99	18.11	20.99	24.06	26.84	
SEVA [90]	13.01	14.32	15.16	14.11	15.65	16.73	16.59	19.27	23.09	
Ours	14.16	15.52	16.45	16.03	17.99	19.32	19.26	22.31	24.52	

**(b) Pose error and chamfer distance  $\downarrow$ .**

Dataset ( $P$ )	RE10K [92] (3)	DL3DV [46] (3)	T&T [38] (3)						
Metric ( $\downarrow$ )	$T_{err}$	$R_{err}$	$CD$	$T_{err}$	$R_{err}$	$CD$	$T_{err}$	$R_{err}$	$CD$
SEVA [90]	1.62	5.84	1.35	35.0	6.44	1.03	6.08	2.87	1.42
Ours	0.76	4.83	0.19	28.3	5.13	0.62	3.56	1.52	0.92

**Table 4 Geometry Fidelity of GeoNVS.**  $T_{err}$ ,  $R_{err}$ , and  $CD$  measure geometric fidelity.  $PSNR_V$  and  $PSNR_U$  denote synthesis quality on co-visible and non-co-visible regions w.r.t. the reference views. All the results are under the Trajectory NVS setting. “Input-level injection” denotes input-level integration of 3D Gaussian priors.

Method	Mip360 Dataset [2] (3 reference views)					DL3DV Dataset [46] (6 reference views)					WRGBD-S <sub>h</sub> Dataset [79] (3 reference views)				
	$T_{err}\downarrow$	$R_{err}\downarrow$	$CD\downarrow$	$PSNR_V\uparrow$	$PSNR_U\uparrow$	$T_{err}\downarrow$	$R_{err}\downarrow$	$CD\downarrow$	$PSNR_V\uparrow$	$PSNR_U\uparrow$	$T_{err}\downarrow$	$R_{err}\downarrow$	$CD\downarrow$	$PSNR_V\uparrow$	$PSNR_U\uparrow$
<b>Baselines</b>															
SEVA [90]	18.76	3.29	0.07	13.85	13.01	19.68	2.80	0.57	15.68	16.90	8.10	8.86	1.58	15.53	15.79
<b>Generative model + VGGT [65] prior</b>															
Difix3D [74]	219.39	51.64	0.68	12.92	11.82	64.4	9.66	3.76	16.11	17.29	19.59	32.48	10.11	11.07	11.36
SEVA + Input-level injection	233.03	99.79	1.02	13.14	12.03	81.14	17.19	3.82	16.76	17.76	29.27	52.51	2.01	11.36	11.42
Ours	16.24	2.98	0.07	15.11	14.07 (+1.06)	13.27	2.01	0.41	18.11	18.98 (+2.08)	4.00	4.56	1.29	17.33	17.51 (+1.72)

**Geometric consistency.** As shown in Tab. 3b, GeoNVS substantially improves geometric consistency over the SEVA baseline across all datasets. This is further corroborated by Tab. 4, where our method consistently outperforms input-level geometry injection approaches — Difix3D [74] and SEVA with input-level injection — by a large margin, demonstrating that feature-space modulation via GS-Adapter is more effective than injecting geometry at the input level.

**Camera controllability.** GeoNVS substantially improves camera controllability over the SEVA baseline. As shown in Tab. 3b and Fig. 8, the gains in synthesis quality stem primarily from improved camera controllability and geometry enhancement, with our method being especially effective in reducing translation deviation. Tab. 4 further supports this: GeoNVS achieves consistently lower pose errors than the SEVA baseline across all three datasets, while competing methods that inject geometry priors at the input level suffer catastrophic degradation in controllability, with translation and rotation errors far exceeding those of the baseline. These results indicate that anchoring diffusion features to explicit 3D structure is key to reliable camera controllability.

**Geometry prior extrapolates to unseen regions.** To evaluate whether geometry priors improve synthesis beyond observed regions, we construct co-visibility masks using VGGT-derived [65] point clouds following the co-visible



**Table 5 GeoNVS with SEVA [90]. Table 6 PSNR  $\uparrow$  on GeoNVS with CameraCtrl [24].** We extend GeoNVS with various geometry priors in a zero-shot manner. All methods are evaluated with 3 reference images.

Method	DTU		CO3D		WRGBD-S <sub>c</sub>		T&T	
	PSNR	SSIM	PSNR	SSIM	PSNR	SSIM	PSNR	SSIM
<b>Baseline</b>								
SEVA [90]	17.03	0.66	17.22	0.55	15.96	0.53	18.85	0.61
<b>Geometry priors</b>								
MVSplat [10]	11.35	0.41	12.04	0.39	12.89	0.41	13.45	0.38
DepthSplat [80]	14.19	0.49	15.08	0.49	13.92	0.44	17.99	0.54
VGGT [65]	17.15	0.64	15.39	0.52	11.09	0.41	23.96	0.81
Pi3 [70]	7.81	0.31	12.60	0.47	10.54	0.37	16.98	0.48
<b>Ours w/ Naïve Fusion</b>								
+ MVSplat	17.04	0.65	18.79	0.62	17.62	0.59	21.18	0.68
+ DepthSplat	17.94	0.68	19.00	0.63	17.97	0.61	22.05	0.71
+ VGGT	18.89	0.69	18.60	0.60	17.60	0.59	22.22	0.70
+ Pi3	14.83	0.59	18.59	0.61	17.38	0.58	21.92	0.69
<b>Ours w/ Adaptive Fusion</b>								
+ MVSplat	19.15	0.69	19.23	0.63	18.22	0.61	22.24	0.69
+ DepthSplat	19.14	0.69	19.24	0.63	18.22	0.61	22.24	0.69
+ VGGT	19.18	0.69	19.26	0.63	18.21	0.61	22.24	0.69
+ Pi3	19.02	0.69	19.22	0.63	18.19	0.61	22.22	0.69

Method	dataset split	CO3D		DTU	RE10K	Mip360	WRGBD	Average
		V	R	R	R	R	S <sub>h</sub>	
<b>Baseline</b>								
CameraCtrl [24]	13.23	11.71	8.72	14.09	10.94	10.38	11.14	
<b>Geometry priors</b>								
MVSplat [10]	10.12	9.14	7.37	11.26	8.55	6.48	8.82	
DepthSplat [80]	11.29	8.54	8.79	14.49	9.20	7.31	9.94	
VGGT [65]	10.48	8.43	7.04	13.94	8.89	6.27	8.67	
Pi3 [70]	12.08	11.80	8.82	11.00	10.60	8.86	10.16	
<b>Ours w/ Naïve Fusion</b>								
+ MVSplat	13.76	12.69	7.71	14.44	11.19	10.63	11.74	
+ DepthSplat	14.64	12.15	11.00	16.85	11.27	10.88	12.80	
+ VGGT	13.30	11.69	8.68	14.08	11.30	10.55	11.60	
+ Pi3	13.60	12.99	8.99	13.35	11.30	10.97	11.87	

**Table 7 Model ablation study of GeoNVS.** We ablate the key components of GS-Adapter, including feature refinement, feature fusion strategy, and multi-scale fusion. All experiments use VGGT [65] as the geometry prior. Here, feats abbreviates features.

Method	GS-Adapter				Mip360		DL3DV		T&T	
	Refinement		Fusion		6-view		6-view		3-view	
	$\mathcal{L}_{\text{feat}}$	GS-PE	Naïve	Adaptive	PSNR $\uparrow$	SSIM $\uparrow$	PSNR $\uparrow$	SSIM $\uparrow$	PSNR $\uparrow$	SSIM $\uparrow$
<b>Geometry prior</b>										
VGGT [65]					15.49	0.362	17.09	0.52	23.96	0.81
<b>Baseline</b>										
SEVA [90]					15.38	0.339	15.84	0.45	18.85	0.61
+ Input-level injection					15.40	0.373	16.73	0.52	23.05	0.74
+ LoRA only					15.55	0.360	17.35	0.54	21.41	0.68
+ GS-Adapter (Encoder-1,2,3 feats)	✓	✓	✓	✓	16.36	0.378	17.80	0.55	21.67	0.69
	✓	✓	✓	✓	16.47	0.378	17.88	0.55	22.11	0.69
	✓	✓	✓	✓	16.48	0.383	17.95	0.56	22.22	0.70
<b>Multi-scale fusion</b>										
+ GS-Adapter (Encoder-1 feat)	✓	✓	✓	✓	16.28	0.376	17.49	0.53	21.36	0.68
+ GS-Adapter (Encoder-1,2 feats)	✓	✓	✓	✓	16.31	0.370	17.53	0.53	21.73	0.68
+ GS-Adapter (Encoder-1,2,3 feats)	✓	✓	✓	✓	16.48	0.383	17.95	0.56	22.22	0.70
<b>Ours (Encoder-1,2,3 feats)</b>	✓	✓	✓	✓	16.57	0.383	18.11	0.56	22.24	0.69

**GeoNVS with CameraCtrl.** To demonstrate that GS-Adapter generalizes beyond SEVA, we integrate it into CameraCtrl [24] in Tab. 6. Standalone geometry priors consistently underperform the CameraCtrl baseline, suggesting that geometry alone is insufficient in sparse-view settings. GeoNVS with Naïve Fusion improves over both the baseline and the standalone priors across most settings, achieving up to +1.66 PSNR gain on average over the baseline, suggesting that GS-Adapter provides complementary benefit even on top of a strong geometry prior and is applicable beyond a single diffusion backbone.

**Analysis of model components.** Table 7 validates the contribution of each design choice in GS-Adapter. Both the feature consistency loss  $\mathcal{L}_{\text{feat}}$  and Gaussian positional encoding (GS-PE) contribute to performance, as removing either component leads to consistent drops across benchmarks, indicating that explicit 3D structural cues and fine-grained supervision are both necessary for recover-

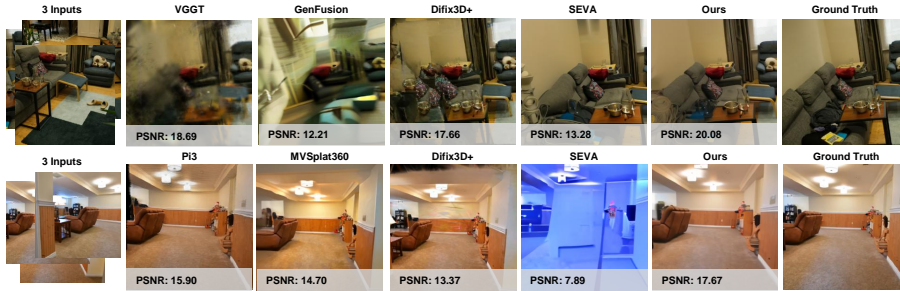


Fig. 6 Qualitative results of GeoNVS with SEVA [90].



Fig. 7 Qualitative results of GeoNVS with CameraCtrl [24]

ing details lost during the lifting-and-rendering process. Finally, using multi-scale features together in GeoNVS provides consistent improvements, indicating that geometry-guided features across multiple spatial resolutions are complementary.

**Comparison with input-level injection of geometry** As shown in Tab. 4, input-level injection of geometry priors causes severe degradation in camera controllability and geometric consistency, performing even worse than the SEVA, a purely generative baseline. This failure stems from the fact that rasterized images introduce view-dependent color noises that corrupt the structural signal rather than reinforcing it. In contrast, the proposed GS-Adapter leverages only the structural information encoded in 3D Gaussians to modulate internal diffusion features, consistently reducing camera pose errors and Chamfer Distance across all datasets. Tab. 7 further reinforces this finding: input-level injection yields synthesis quality gains only when the geometry prior is near-perfect, whereas GS-Adapter consistently improves PSNR regardless of prior quality. These results collectively demonstrate that feature-level geometry modulation is both more robust and more effective than image-level injection.

**Pose-free experiment.** We extend GeoNVS to unknown pose scenarios by integrating ViPE [27], which outperforms VGGT [65] in robustness on complex scenes. Given poses estimated by ViPE from input images, we optimize 3D-GS using VGGT point cloud, with scale aligned to ViPE poses solved via Eq. (1). As shown in the **right table**, GeoNVS maintains high synthesis ability without requiring ground-truth intrinsics or extrinsics. On T&T [38], the ViPE pose setting slightly outperforms the GT pose setting, which we attribute to ViPE’s more robust estimation compared to the noisy COLMAP [60, 61]-derived poses in the T&T dataset.

Dataset ( $P$ )	DL3DV (6)			T&T (3)		
	$T_{err}$	$R_{err}$	PSNR	$T_{err}$	$R_{err}$	PSNR
<b>w/ GT Pose</b>						
SEVA [90]	19.68	2.80	15.64	6.08	2.87	18.63
<b>Ours</b>	<b>13.27</b>	<b>2.01</b>	<b>17.99</b>	3.56	<b>1.52</b>	22.24
<b>w/ ViPE [27] Pose</b>						
SEVA [90]	25.11	3.54	15.38	2.73	4.87	19.24
<b>Ours</b>	20.64	2.98	17.87	<b>1.05</b>	2.40	<b>22.31</b>

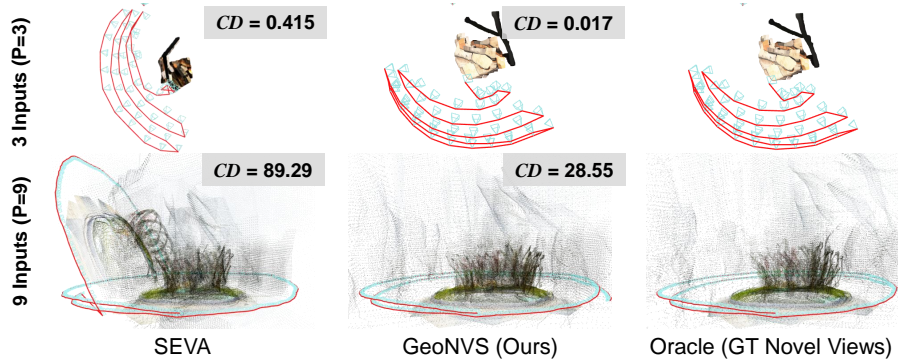
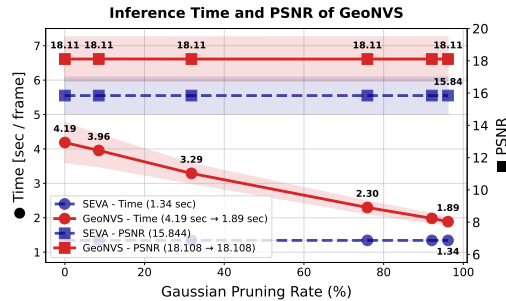


**Fig. 8 Qualitative results of GeoNVS.** 3D reconstruction and camera trajectory estimated from the generated video, showing the improved geometric fidelity of GeoNVS.

**Runtime complexity and acceleration.** We measure inference time and PSNR across 10 scenes from DL3DV-10K to analyze the computational overhead relative to SEVA. As shown in the Figure below, the primary bottleneck is the number of Gaussians from the geometry prior, which increases inference time to 4.19 sec/frame without pruning. However, applying voxel-based Gaussian pruning [32] reduces inference time to 1.89 sec/frame at a 96.2% pruning rate, achieving a 2.22 $\times$  speedup, while maintaining PSNR advantage of +2.27 dB over SEVA.



## 5 Conclusions

We present GeoNVS, a geometry-grounded novel-view synthesizer that enhances geometric fidelity and camera controllability using GS-Adapter. Unlike prior methods that inject geometry at the input level, GS-Adapter modulates internal diffusion features using 3D Gaussian priors in a plug-and-play manner, enabling zero-shot compatibility with any geometry model and diffusion backbone. Extensive experiments across 9 scenes and 18 settings demonstrate state-of-the-art performance, achieving 11.3% and 14.9% improvements over SEVA and CameraCtrl, with up to 2 $\times$  reduction in translation error and 7 $\times$  in Chamfer Distance. GeoNVS improves synthesis in non-co-visible regions by up to 2.08 dB, confirming that feature-level 3D grounding facilitates extrapolation beyond observed regions. Finally, GeoNVS supports pose-free scenarios via SfM methods [18, 27] and reduces inference overhead by 2.2 $\times$  with negligible performance degradation.

**Limitations and future work.** While our proposed method demonstrates impressive performance in sparse-view settings and long-range trajectory NVS, its generation ability degrades in regions distant from input views. We attribute this to increasingly uncertain feature rendering in GS-Adapter as the distance from input views grows. One of the promising directions for future work is to incorporate uncertainty estimation for 3D-GS [23] to address this limitation.

## Supplementary Material

This supplementary material is organized as follows.

- Sec. **A** summarizes the mathematical notation used throughout the paper.
- Sec. **B** provides details on dataset splits and comparison methods.
- Sec. **C** presents additional experiments, including ablations on input-level injection strength, feature uplifting, and adaptive fusion gating analysis.
- Sec. **D** describes the detailed architectures of the multi-scale fusion module and RefineNet.
- Sec. **E** explains the training dataset preprocessing pipeline.
- Sec. **F** provides additional quantitative results in SSIM and LPIPS.
- Sec. **G** presents additional qualitative results across diverse settings.
- Sec. **H** discusses limitations and failure cases of GeoNVS.

### A Notation Table

Tab. 10 summarizes the mathematical notation used in the paper by category.

### B Detail of Evaluation Benchmark

We evaluate GeoNVS across 9 scenes and 18 settings drawn from 8 public benchmarks following SEVA [90]: OmniObject3D [77], RealEstate10K [92], LLFF [51], DTU [30], CO3D [57], WRGBD [79], Mip-NeRF 360 [2], DL3DV [46], and Tanks and Temples [38]. We detail the dataset splits and evaluation protocols of comparison methods in Secs. B.1 and B.2.

#### B.1 Dataset Splits

The data splits used in the evaluation tables include ReconFusion [75] (R), 4DiM [72] (D), SEVA [90] (S), pixelSplat [8] (P), ViewCrafter [86] (V), LongLRM [94] (L), and our own split referred from CF-3DGS [18] (O).

#### B.2 Evaluation Details of Comparison Methods

**MVSplat [10], HiSplat [63], DepthSplat [80].** We use these feed-forward methods to directly regress Gaussian splats  $\mathcal{G}$  from the input-view images  $\mathbf{I}_{\text{ref}}$ . These methods require posed images (images with corresponding poses  $\boldsymbol{\pi}$ ).

**VGGT [65], Pi3 [70].** Using the point cloud and camera parameters predicted by the feed-forward methods, we initialize the Gaussian splats  $\mathcal{G}$  directly from the point cloud. We then apply the co-visibility-based redundancy elimination strategy of InstantSplat [17] to prune overlapping regions, and further optimize the 3D-GS representation [35] with the reference view images  $\mathbf{I}_{\text{ref}}$ . The scale ambiguity between the predicted camera poses and the ground-truth point cloud is resolved using Eq. (1).

**ViewCrafter [86].** In the original implementation, ViewCrafter operates in an exploratory manner without any knowledge of target viewpoints, relying on dust3r [68] to estimate camera parameters and iteratively expanding the point cloud with generated frames. For evaluation, we instead provide ground-truth camera poses and use  $P$  reference views alongside 5 additional viewpoints for geometry estimation, then render along the ground-truth trajectory before passing to the diffusion model. Note that this setting provides an advantage over the original by eliminating camera estimation error, and thus can be regarded as an upper-bound approximation of ViewCrafter’s performance.

**MotionCtrl** [71]. We employ only the CMCM module from MotionCtrl for camera control, following the original inference protocol with 25 denoising steps and the same classifier-free guidance scale. All videos are generated at  $576 \times 1024$  resolution and resized to  $384 \times 384$  for evaluation.

**CameraCtrl** [24]. We use the SVD [3] based CameraCtrl officially provided by the author. The inference process follows the original paper, using 25 steps and the same conditional-guidance scale. All videos are generated at a resolution of  $320 \times 576$  and subsequently resized to  $384 \times 384$  for evaluation.

**SEVA** [90]. We adopt the officially released v1.0 model provided by the authors; our GeoNVS framework is similarly built upon SEVA v1.0. Inference is performed following the settings of the original paper, using 50 denoising steps with a CFG scale of 2.0. All videos are rendered at a resolution of  $384 \times 384$ .

**MVSplat360** [11]. We first render novel-view features from MVSplat and use these features as input to generate novel-view images using SVD, following the original implementation.

**GenFusion** [76]. Rather than adopting GenFusion’s direct 3D reconstruction pipeline, we first leverage geometry priors from a regression-based model to render novel-view RGB, depth (RGBD) images. These noisy RGBD predictions are then fed into GenFusion for refinement. All videos are generated at a resolution of  $320 \times 512$  and subsequently resized to  $384 \times 384$  for evaluation.

**Difix3D** [74]. We utilize the Difix3D model by providing a reference image together with the novel-view image rendered by the geometry prior (regression-based model). The reference image is chosen from the input-view set  $I_{IV}$  based on the camera-center distance to the target novel-view viewpoint.

### B.3 Geometry prior used for combined methods

For fair comparison, all combined methods [74, 76] and ours use the best-performing geometry prior per dataset in Tab. 1. Tab. 9 lists the geometry priors used in each benchmark for small-viewpoint NVS. Note that MVSplat360 [11] is an exception, as it is limited to MVSplat [10] by design.

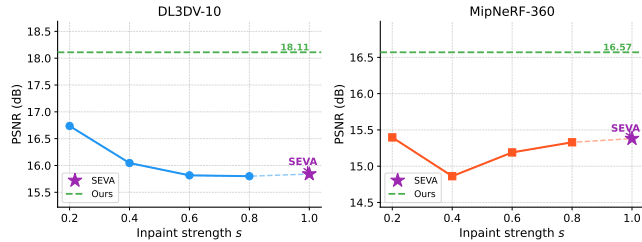
**Table 9** Geometry prior used for combined methods of small-viewpoint NVS in Tab. 1.

Benchmark	Input number ( $P$ )	Geometry prior
OO3D [77]-S	3	DepthSplat [80]
RE10K [92]-D	1	DepthSplat [80]
RE10K [92]-P	2	DepthSplat [80]
RE10K [92]-R	1	DepthSplat [80]
RE10K [92]-R	3	Pi3 [70]
LLFF [51]-R	1, 3	VGGT [65]
DTU [30]-R	1	Pi3 [70]
DTU [30]-R	3	VGGT [65]
CO3D [57]-V	1	Pi3 [70]
CO3D [57]-R	3	VGGT [65]
WRGBD [79]- $S_e$	3	DepthSplat [80]
WRGBD [79]- $S_h$	6	DepthSplat [80]
Mip360 [2]-R	6	VGGT [65]
DL3DV [46]-S	6	VGGT [65]
DL3DV [46]-L	9	VGGT [65]
T&T [38]-O	2, 3	VGGT [65]

## C Additional Experiments

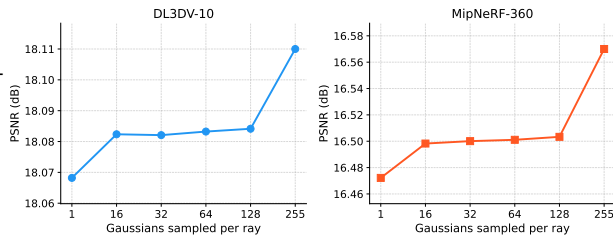
### C.1 Injection Strength in Input-Level Integration

To ensure a fair comparison with input-level injection approaches, we analyze performance across different inpaint strength levels  $s$ , where smaller  $s$  enforces stronger adherence to the geometry prior and larger  $s$  approaches the purely generative baseline [90]. As shown in Fig. 10, input-level injection performs best at small  $s$  on DL3DV-10K, where the geometry prior dominates, but degrades monotonically as  $s$  increases toward the generative baseline. On MipNeRF-360, performance is unstable across all  $s$  values, suggesting that noisy rasterized colors corrupt the structural signal regardless of inpaint strength. In contrast, GS-Adapter consistently outperforms input-level injection across all  $s$  values on both datasets, demonstrating that feature-level modulation yields more stable and consistently superior results regardless of the geometry prior strength.



### C.2 Ablation on Feature Uplifting: Point Cloud vs 3D-GS

In the feature uplifting process, restricting each ray to consider only the single Gaussian with the highest rendering weight reduces the process to a **hard assignment** scheme, in which each pixel’s feature is attributed solely to the most opaque surface point along that ray, which is mathematically equivalent to projecting features onto a point cloud. In contrast, the **soft assignment** scheme in Eq. (4) aggregates all Gaussians along a ray as a rendering-weight-proportional weighted sum, following the same principle as alpha-compositing to continuously accumulate features across the volume. This formulation mitigates the fragility of hard assignment in regions where multiple Gaussians partially contribute to a single pixel, as a single dominant Gaussian may fail to capture the full structural signal of the scene. Since Gaussians with moderate rendering weights are entirely discarded under hard assignment, soft assignment ensures that all contributing Gaussians accumulate feature information proportional to their geometric relevance, yielding a smoother and more consistent feature field upon rasterization into novel views and ultimately improving both geometric consistency and synthesis quality. We validate this in Figure above by varying  $k \in \{1, 16, 32, 64, 128, 255\}$  on Mip-NeRF 360 and DL3DV-10K, where  $k=1$  and  $k=255$  correspond to hard and full soft assignment, respectively. PSNR consistently improves with increasing  $k$  on both datasets, confirming the effectiveness of soft assignment.



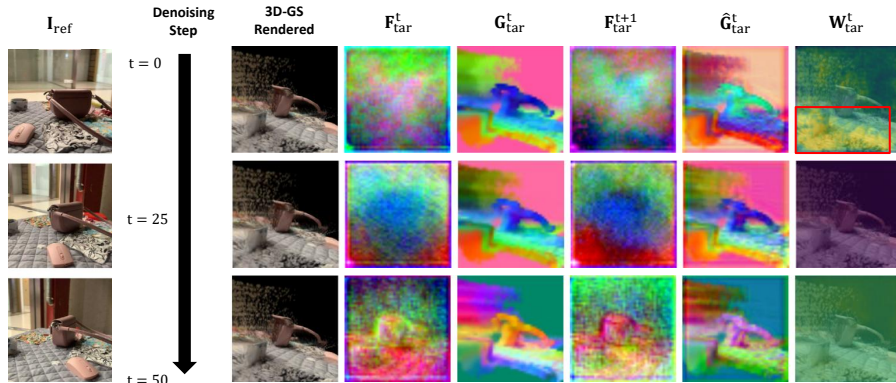


Fig. 12 Visualization of intermediate features in GeoNVS.

### C.3 Gate Analysis of Adaptive Fusion

We visualize intermediate features throughout the denoising process in Fig. 12. At early denoising steps ( $t=0$ ), the diffusion features  $\mathbf{F}_{\text{tar}}^t$  are spatially incoherent due to high noise levels, while the rendered Gaussian features  $\mathbf{G}_{\text{tar}}$  consistently exhibit sharp structures derived from the 3D geometry prior. Notably, the gating weight  $\mathbf{W}_{\text{tar}}^t$  at  $t=0$  concentrates high values on geometrically salient regions (red box), indicating that adaptive fusion heavily relies on the geometry prior to correct the noisy diffusion features at the early stage. As denoising progresses toward  $t=50$ ,  $\mathbf{F}_{\text{tar}}^t$  progressively recovers structural coherence, and  $\mathbf{W}_{\text{tar}}^t$  transitions to a more spatially uniform distribution, reflecting a natural shift from geometry-driven correction to generative refinement. These observations confirm that GS-Adapter adaptively balances geometric guidance and generative capability throughout the denoising process, anchoring diffusion features to explicit 3D geometry when needed while preserving the generative model’s flexibility in later steps.

## D Model Architecture Details

Detailed descriptions of the multi-scale fusion module and the RefineNet  $\mathcal{R}$  used in the feature refinement of GS-Adapter are provided in Sec. 3.3 and Sec. 3.2.

### D.1 Multi-Scale Fusion

The detailed architecture of the multi-scale fusion module in GeoNVS is illustrated in Fig. 13. This module aggregates multi-scale features from the diffusion module to produce a single feature map at a unified resolution.

### D.2 RefineNet Architecture

The detailed architecture of the RefineNet module in GS-Adapter is illustrated in Fig. 14. This module takes the rasterized Gaussian feature  $\mathbf{G}$  as input and produces a refined feature representation  $\hat{\mathbf{G}}$ .

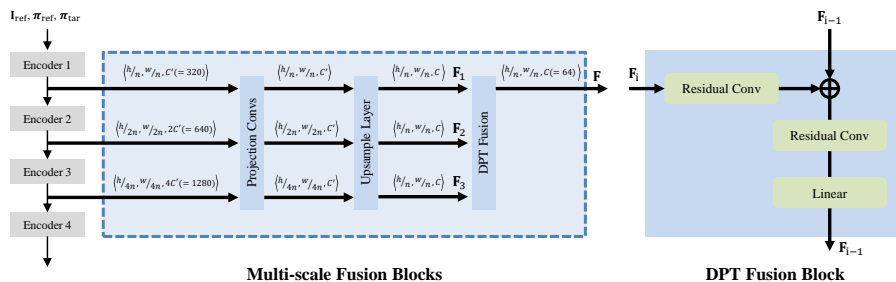
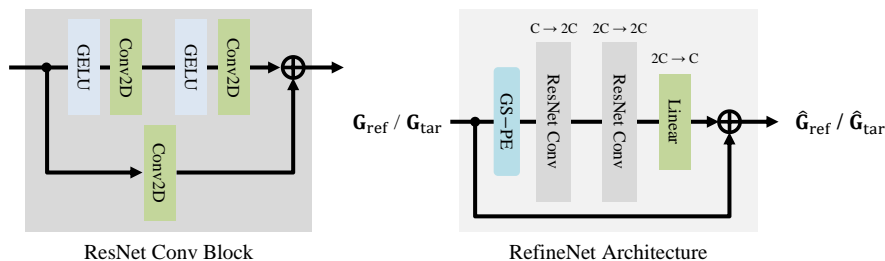


Fig. 13 Multi-scale fusion module of GeoNVS.

Fig. 14 RefineNet module ( $\mathcal{R}$ ) of GS-Adapter.

## E Training Dataset Preprocessing

We construct our training dataset from DL3DV-10K [46] by preprocessing each scene into input–target view pairs annotated with pretrained 3D Gaussian representations. Images are resized to  $480 \times 270$  or  $960 \times 540$  resolution, and camera poses are converted to world-to-camera extrinsics with normalized intrinsics. For structured view selection in Algorithm 1, we construct a pose graph over all frames using pairwise combined pose distances [14] and connect frames within a dynamic distance threshold that guarantees at least  $N_{\text{group}} = 21$  near neighbors per frame. Anchor nodes are sampled proportionally to their graph degree, yielding  $K = 3$  independent view groups per scene. Within each group, input views ( $P \in \{1, 3, 6, 9, 12\}$ ) are selected via K-means clustering on camera position and orientation to maximize spatial diversity. The remaining frames serve as novel-view candidates and are divided into *easy* and *hard* subsets based on their minimum CLIP cosine distance [55] to the input views, where the bottom 60% by distance constitute easy samples. Both subsets are filtered by a frustum IoU threshold of  $\tau_{\text{IoU}} = 0.4$  to ensure sufficient overlap between input and target cameras. Each resulting input–target pair is then processed by VGGT [65] to obtain an initial point cloud, which is further optimized into 3D Gaussians given the reference images, parameterized by position  $\mu$ , rotation quaternion  $\mathbf{q}$ , scale  $\mathbf{s}$ , opacity  $\alpha$ , and spherical harmonic coefficients.

---

**Algorithm 1** View Selection for Novel View Synthesis

---

**Require:** Images  $\mathcal{I}$  with camera poses  $\{\pi_i\}_{i=1}^{P+Q}$ , number of anchors  $V$ , group size  $N_g$ , input view count  $P$ , frustum IoU threshold  $\tau$

**Ensure:** Set of (input, target) view pairs  $\mathcal{P}$

1: **Step 1: Build pose-distance graph**

2: Compute pairwise pose distance for all  $(i, j)$ :

$$d(i, j) = \sqrt{\|\mathbf{t}_{ij}\|^2 + 2\left(1 - \frac{\text{tr}(\mathbf{R}_{ij})}{3}\right)}$$

3: Set threshold  $\delta$  s.t. each node has at least  $N_g$  neighbors

4: Construct graph  $G=(\mathcal{V}, \mathcal{E})$  where  $(i, j) \in \mathcal{E}$  iff  $d(i, j) < \delta$

5: **Step 2: Sample anchor nodes**

6: Sample  $V$  anchors weighted by graph degree

7: **Step 3: Generate (input, target) pairs**

8:  $\mathcal{P} \leftarrow \emptyset$

9: **for** each anchor  $a_k$  **do**

10:  $\Omega_k \leftarrow \{a_k\} \cup \mathcal{N}_G(a_k)$

11: Select input views  $\mathcal{S}_{\text{in}}$  via K-Means on  $[\mathbf{c}_i \|\hat{\mathbf{d}}_i]$

12: Partition remaining views into  $\mathcal{C}_{\text{easy}} / \mathcal{C}_{\text{hard}}$  by CLIP distance to  $\mathcal{S}_{\text{ref}}$

13: Select easy targets via K-Means; select hard targets via random sampling

14: Filter both by  $\text{FrustumIoU}(\cdot, \mathcal{S}_{\text{ref}}) \geq \tau$

15:  $\mathcal{P} \leftarrow \mathcal{P} \cup \{(\mathcal{S}_{\text{ref}}, \mathcal{S}_{\text{tar}})\}$

16: **end for**

17: **return**  $\mathcal{P}$ 

---

## F Additional Quantitative Results

We provide additional SSIM and LPIPS results:

- **Small-viewpoint set NVS** in Tab. 11, corresponding to Tab. 1.
- **Large-viewpoint set NVS** in Tab. 12, corresponding to Tab. 2a.
- **Long trajectory NVS** in Tab. 13, corresponding to Tab. 3a.

## G Additional Qualitative Results

We provide additional qualitative results:

- **Small-viewpoint set NVS** in Figs. 15 to 18, corresponding to Tab. 1.
- **Large-viewpoint set NVS** in Figs. 19 and 20, corresponding to Tab. 2a.
- **GeoNVS with CameraCtrl** in Fig. 22, corresponding to Tab. 6.
- **GeoNVS with geometry priors** in Fig. 21, corresponding to Tab. 5.
- **Trajectory NVS with ViPE [27] Reconstruction** in Figs. 23 and 24, corresponding to Tab. 3b.
- **Input-level injection vs Ours** in Fig. 25, corresponding to Tab. 4.

## H Limitations and Failure Cases

As shown in Fig. 26, GeoNVS exhibits two main failure modes. First, geometry inconsistency arises in thin structures such as poles and fences, where sparse Gaussian representations fail to accurately capture fine-grained geometry, propagating errors into the rendered novel-view features. Second, blurry textures appear in heavily occluded regions invisible from any reference view, where insufficient geometric guidance leaves the diffusion model to hallucinate plausible but blurry content. Incorporating uncertainty-aware Gaussian representations or inpainting-based priors for occluded regions remains a promising direction for future work.

Table 10 Notation Table for GeoNVS.

Notation	Description
<b>Scene &amp; Camera</b>	
$P, Q$	Number of reference (input) views and target novel views
$\mathbf{I}_{\text{ref}}, \mathbf{I}_{\text{tar}}$	Reference view, target novel-view RGB images
$\boldsymbol{\pi}^{\text{ref}}, \boldsymbol{\pi}^{\text{tar}}$	Camera poses of reference views and target views
$s^*$	Scale aligning predicted cameras to target cameras
$\mathbf{C}^{\text{gt}}, \mathbf{C}^{\text{pred}}$	Ground-truth and predicted camera centers
<b>3D Gaussian Splatting</b>	
$\mathcal{G}$	Set of 3D Gaussians
$N$	Total number of Gaussian particles
$\boldsymbol{\mu} \in \mathbb{R}^3$	3D position of a Gaussian
$\mathbf{r} \in \mathbb{R}^4$	Rotation of a Gaussian (quaternion)
$\mathbf{s} \in \mathbb{R}^3$	Scale of a Gaussian
$\sigma \in \mathbb{R}^1$	Opacity of a Gaussian
$C(d, p)$	Rendered color at pixel $p$ for view direction $d$
$c_i(d)$	View-dependent color of the $i$ -th Gaussian
$w_i$	Rendering (blending) weight of the $i$ -th Gaussian
$\alpha_i$	Product of opacity $\sigma_i$ and 2-D projected Gaussian density
$\mathbf{f}_i$	Per-Gaussian feature vector
<b>GS-Adapter &amp; Diffusion Features</b>	
$n$	VAE spatial downsampling factor
$C$	Channel dimension of diffusion features
$\mathbf{F}^t$	Diffusion features at denoising timestep $t$
$\mathbf{F}_{\text{ref}}^t \in \mathbb{R}^{P \times \frac{h}{n} \times \frac{w}{n} \times C}$	Reference-view diffusion features at timestep $t$
$\mathbf{F}_{\text{tar}}^t \in \mathbb{R}^{Q \times \frac{h}{n} \times \frac{w}{n} \times C}$	Novel-view diffusion features at timestep $t$
$\hat{\mathbf{F}}^i$	Geometry-augmented diffusion features
$\tilde{\mathbf{f}}_i \in \mathbb{R}^C$	$\ell_2$ -normalized uplifted feature of the $i$ -th Gaussian
$\mathbf{G}_{\text{tar}} \in \mathbb{R}^{Q \times \frac{h}{n} \times \frac{w}{n} \times C}$	Rasterized geometry-constrained novel-view features
$i^*(d, p)$	Index of the most contributing Gaussian at pixel $(d, p)$
$\tilde{\mathbf{x}}(d, p) = (\tilde{x}, \tilde{y}, \tilde{z})$	Normalized 3D center of $i^*(d, p)$
$w^*(d, p)$	Rendering weight of the dominant Gaussian $i^*(d, p)$
$\gamma(\cdot)$	Sinusoidal positional encoding
$D' = C/4$	Encoding dimension for positional encoding
$\omega_k = \omega_0^{-2k/D'}$	Frequency for the $k$ -th sinusoidal component
$\mathbf{G}'(d, p)$	Positionally-encoded Gaussian feature (GS-PE applied)
$\mathcal{R}$	ResNet-based feature refinement network
$\mathcal{P}$	MLP projection applied after refinement
$\hat{\mathbf{G}} = \mathcal{R}(\mathbf{G}')$	Refined Gaussian features
$\hat{\mathbf{G}}_{\text{ref}} \in \mathbb{R}^{P \times \frac{h}{n} \times \frac{w}{n} \times C}$	Refined reference-view Gaussian features
$\hat{\mathbf{G}}_{\text{tar}} = \mathcal{P}(\hat{\mathbf{G}}_{\text{tar}})$	Projected refined novel-view features
$\mathbf{F}_{\text{tar}}^A$	Geometry-attended features via cross-attention
$\mathbf{W}_{\text{tar}} \in [-1, 1]$	Pixel-wise confidence gate weight
$\hat{\mathbf{F}}_{\text{tar}}$	Final geometry-augmented novel-view features
<b>Loss Functions</b>	
$\mathcal{L}_{\text{feat}}$	Feature consistency loss
$\mathcal{L}_{\text{latent}}$	Latent space alignment loss
<b>Evaluation Metrics</b>	
$T_{\text{err}}$ [cm]	Camera translation error
$R_{\text{err}}$ [deg]	Camera rotation error
$CD$	Chamfer Distance between reconstructed point clouds
$\text{PSNR}_V$	PSNR on co-visible regions w.r.t. reference views
$\text{PSNR}_U$	PSNR on non-co-visible (unseen) regions

**Table 11 Small-viewpoint set NVS.** We report SSIM and LPIPS metrics corresponding to Tab. 1 of the manuscript.  $P$  denotes the number of reference images. For  $P=1$ , we sweep the unit length for camera normalization following [90] to resolve scale ambiguity. For each dataset, all combined (generative + geometry) methods use the top-performing feed-forward geometry model by PSNR as the geometry prior.

(a) SSIM  $\uparrow$  on small-viewpoint set NVS.

Method	dataset	OO3D [77]		RE10K [92]			LLFF [51]		DTU [30]		CO3D [57]		WRGBD [79]		Mip360 [2]	DL3DV [46]		T&T [38]		Average
	split	S	D	P	R		R		R		V	R	S <sub>c</sub>	S <sub>b</sub>	R	S	L	O		
	$P$	3	1	2	1	3	1	3	1	3	1	3	3	6	6	6	9	2	3	
<b>Feed-forward geometry models</b>																				
MVSplat [10]		0.879	0.317	0.868	0.364	0.870	0.003	0.323	0.140	0.409	0.237	0.390	0.406	0.393	0.239	0.379	0.427	0.333	0.377	0.409
HiSplat [63]		0.877	0.444	<b>0.872</b>	0.540	0.902	0.01	0.384	0.149	0.467	0.286	0.434	0.434	0.419	0.290	0.419	0.457	0.360	0.468	0.456
DepthSplat [80]		0.897	0.468	0.868	0.529	<b>0.918</b>	0.02	0.332	0.262	0.485	0.337	0.492	0.441	0.434	0.303	0.465	0.528	0.472	0.535	0.488
VGGT [65] + InstantSplat [17]		0.892	0.499	0.798	0.561	0.914	0.234	<b>0.672</b>	0.215	0.640	0.297	0.524	0.409	0.432	0.362	0.518	0.571	<b>0.716</b>	<b>0.807</b>	0.559
Pi3 [70] + InstantSplat [17]		0.857	0.392	0.807	0.452	0.910	0.180	0.374	0.356	0.314	0.420	0.470	0.371	0.385	0.277	0.455	0.523	0.406	0.475	0.468
<b>Generative models</b>																				
MotionCtrl [71]		-	0.502	-	0.592	-	0.314	-	0.401	-	0.452	-	-	-	-	-	-	-	-	0.452
CameraCtrl [24]		-	0.491	-	0.578	-	0.294	-	0.400	-	0.451	-	-	-	-	-	-	-	-	0.443
ViewCrafter [86]		0.861	0.551	-	<b>0.693</b>	0.647	0.283	0.253	0.370	0.274	0.520	0.300	0.233	0.215	0.194	0.241	0.230	0.286	0.300	0.379
SEVA [90]		<b>0.926</b>	0.534	0.777	0.616	0.842	0.294	0.467	0.430	0.659	0.507	0.551	0.527	0.522	0.339	0.450	0.513	0.521	0.608	0.560
<b>Generative model + Geometry prior</b>																				
MVSplat360 [11]		0.884	0.518	0.756	0.574	0.817	0.314	0.419	0.366	0.517	0.459	0.555	0.514	0.483	0.327	0.471	0.524	0.467	0.535	0.528
GenFusion [76]		0.876	0.559	0.818	0.618	0.864	0.271	0.554	0.355	0.556	0.438	0.449	0.453	0.425	0.282	0.394	0.492	0.630	0.689	0.540
Difix3D [74]		0.898	0.463	0.857	0.528	0.903	0.230	0.638	0.342	0.637	0.375	0.479	0.350	0.333	0.301	0.481	0.519	0.696	0.779	0.545
GeoNVs (Ours)		0.904	<b>0.612</b>	0.826	0.680	0.895	<b>0.346</b>	0.514	<b>0.480</b>	<b>0.691</b>	<b>0.550</b>	<b>0.627</b>	<b>0.607</b>	<b>0.577</b>	<b>0.383</b>	<b>0.562</b>	<b>0.635</b>	0.603	0.695	<b>0.622</b>

(b) LPIPS  $\downarrow$  on small-viewpoint set NVS.

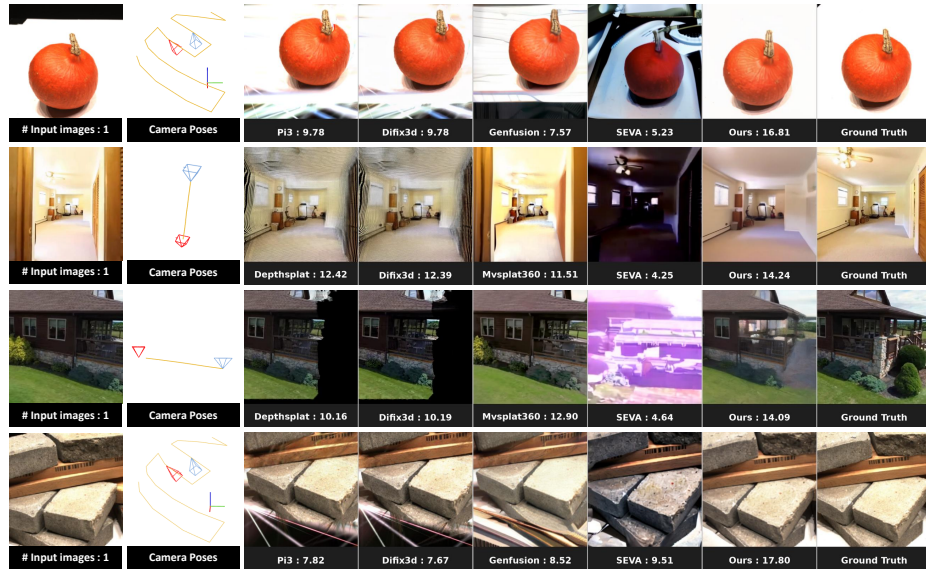
Method	dataset	OO3D [77]		RE10K [92]			LLFF [51]		DTU [30]		CO3D [57]		WRGBD [79]		Mip360 [2]	DL3DV [46]		T&T [38]		Average
	split	S	D	P	R		R		R		V	R	S <sub>c</sub>	S <sub>b</sub>	R	S	L	O		
	$P$	3	1	2	1	3	1	3	1	3	1	3	3	6	6	6	9	2	3	
<b>Feed-forward geometry models</b>																				
MVSplat [10]		0.152	0.643	0.098	0.615	0.134	1.04	0.514	0.816	0.516	0.662	0.592	0.494	0.615	0.673	0.614	0.630	0.566	0.533	0.550
HiSplat [63]		0.155	0.522	0.110	0.484	0.094	1.02	0.479	0.783	0.483	0.645	0.581	0.496	0.610	0.691	0.627	0.650	0.612	0.474	0.529
DepthSplat [80]		0.134	0.444	0.100	0.414	0.074	0.979	0.351	0.550	0.362	0.553	0.498	0.431	0.493	0.552	0.487	0.477	0.332	0.235	0.415
VGGT [65] + InstantSplat [17]		0.172	0.441	0.138	0.454	0.078	0.517	<b>0.153</b>	0.779	0.340	0.608	0.530	0.696	0.623	0.618	0.466	0.497	<b>0.194</b>	<b>0.127</b>	0.413
Pi3 [70] + InstantSplat [17]		0.294	0.701	0.136	0.684	0.087	0.691	0.328	0.666	0.727	0.593	0.643	0.652	0.675	0.660	0.467	0.503	0.406	0.311	0.512
<b>Generative models</b>																				
MotionCtrl [71]		-	0.502	-	0.478	-	0.738	-	0.664	-	0.518	-	-	-	-	-	-	-	-	0.580
CameraCtrl [24]		-	0.514	-	0.492	-	0.610	-	0.611	-	0.540	-	-	-	-	-	-	-	-	0.553
ViewCrafter [86]		0.211	0.405	-	<b>0.338</b>	0.385	0.527	0.562	0.634	0.690	0.425	0.727	0.715	0.727	0.675	0.649	0.680	0.542	0.516	0.553
SEVA [90]		<b>0.062</b>	0.400	0.131	0.402	0.095	0.469	0.212	0.524	0.210	0.399	0.333	0.339	0.331	0.367	0.305	0.288	0.238	0.164	0.293
<b>Generative model + Geometry prior</b>																				
MVSplat360 [11]		0.153	0.454	0.203	0.471	0.164	0.581	0.413	0.731	0.485	0.581	0.525	0.436	0.487	0.556	0.380	0.410	0.445	0.348	0.435
GenFusion [76]		0.158	0.408	0.183	0.384	0.159	0.554	0.301	0.702	0.430	0.621	0.616	0.507	0.577	0.655	0.537	0.520	0.278	0.223	0.434
Difix3D [74]		0.106	0.447	<b>0.097</b>	0.422	0.083	0.520	<b>0.153</b>	0.648	0.240	0.544	0.456	0.508	0.549	0.425	0.313	0.326	<b>0.158</b>	<b>0.101</b>	0.339
GeoNVs (Ours)		0.074	<b>0.325</b>	0.113	<b>0.319</b>	<b>0.071</b>	0.412	0.208	<b>0.449</b>	<b>0.174</b>	<b>0.393</b>	<b>0.279</b>	<b>0.275</b>	<b>0.290</b>	<b>0.329</b>	<b>0.245</b>	<b>0.235</b>	0.225	0.138	<b>0.253</b>

**Table 12 Large-viewpoint set NVS.** The large-viewpoint set contains scenes with low view overlap between reference and target views.  $P$  denotes the number of reference images. We use DepthSplat [80] as the geometry prior for both combined methods.

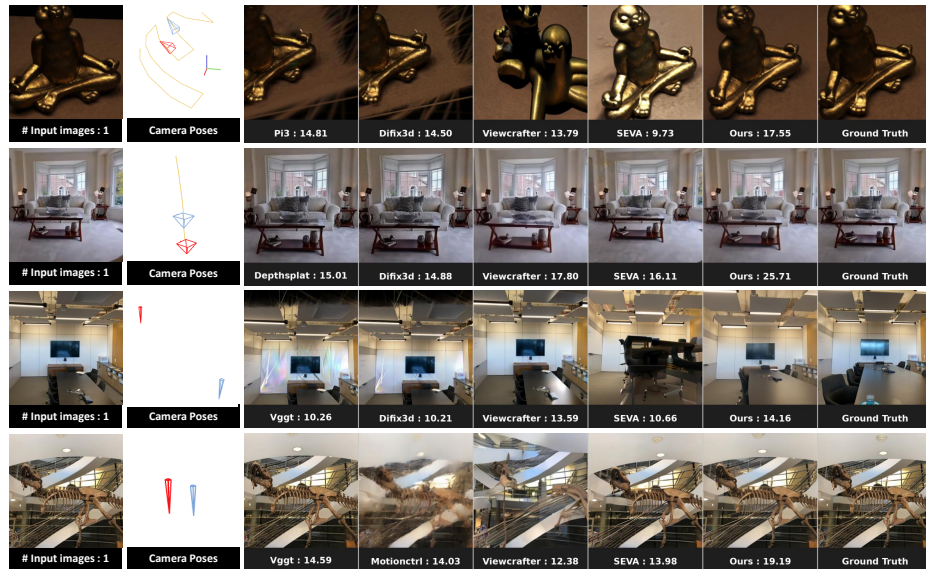
(a) SSIM $\uparrow$ results.								(b) LPIPS $\downarrow$ results.							
Method	dataset		CO3D [57]			WRGBD [79]			Mip360 [2]			DL3DV [46]			Average
	split	$P$	R	$S_h$	S	R	$S_h$	S	R	$S_h$	S	R	$S_h$	S	
<b>Geometry prior</b>															
DepthSplat [80]		1	1	3	1	3	1	3	1	3	1	3	1	3	0.216
<b>Generative models</b>															
MotionCtrl [71]		1	0.461	0.412	-	0.284	-	0.318	-	0.369					
CameraCtrl [24]		1	0.456	0.382	-	0.249	-	0.307	-	0.349					
ViewCrafter [86]		1	0.384	-	0.231	0.222	0.190	0.271	0.229	0.255					
SEVA [90]		1	0.428	0.382	0.455	0.235	0.318	0.543	0.390	0.393					
<b>Generative model + Geometry prior</b>															
GenFusion [76]		1	0.346	0.302	0.370	0.190	0.253	0.262	0.390	0.302					
Difix3D+ [74]		1	0.182	0.170	0.337	0.077	0.248	0.089	0.388	0.213					
GeoNVS (Ours)		1	0.534	0.442	0.507	0.276	0.352	0.370	0.480	0.430					

**Table 13 Long trajectory.** The long trajectory NVS measures the long-term generation ability of generative NVS.  $P$  denotes the number of reference images. We use VGGT [65] as the geometry prior for our method.

(a) SSIM $\uparrow$ results.											(b) LPIPS $\downarrow$ results.											
Method	dataset	$P$	Mip360 [2]			DL3DV [46]			T&T [38]			dataset	$P$	Mip360 [2]			DL3DV [46]			T&T [38]		
			3	6	9	3	6	9	2	3	6			3	6	9	3	6	9	2	3	6
DepthSplat [80]		1	0.277	0.292	0.310	0.415	0.464	0.490	0.474	0.530	0.552		1	0.644	0.593	0.560	0.547	0.494	0.464	0.376	0.301	0.259
VGGT [65]		1	0.305	0.351	0.383	0.466	0.515	0.537	0.718	0.809	0.860		1	0.659	0.633	0.645	0.466	0.469	0.488	0.193	0.126	0.124
SEVA [90]		1	0.302	0.326	0.343	0.384	0.442	0.479	0.534	0.614	0.721		1	0.479	0.417	0.378	0.400	0.315	0.262	0.241	0.175	0.112
Ours		1	0.341	0.372	0.395	0.485	0.559	0.607	0.628	0.712	0.763		1	0.341	0.370	0.329	0.343	0.253	0.206	0.197	0.137	0.105

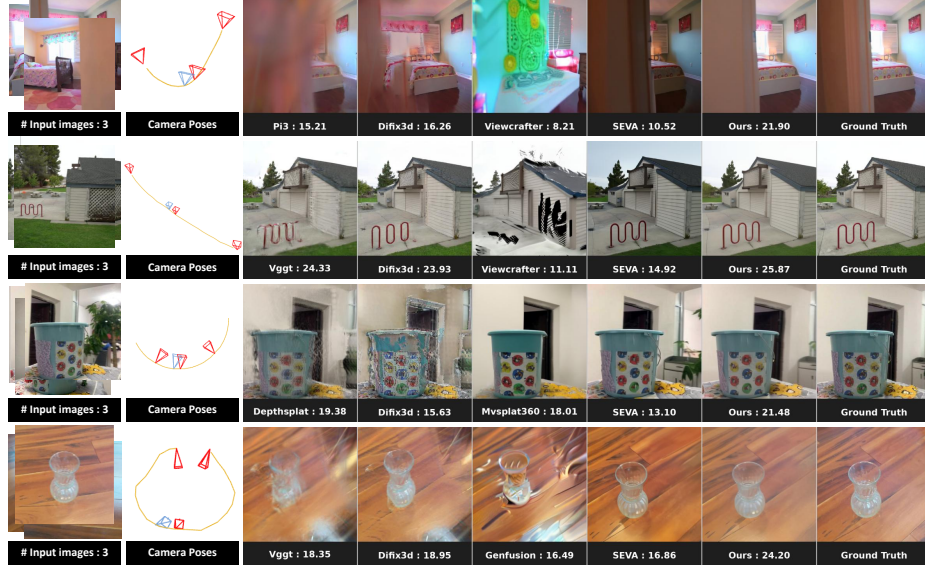


(a) Qualitative results. Given sparse **reference-view** images, novel-view images are synthesized at **target viewpoints**.

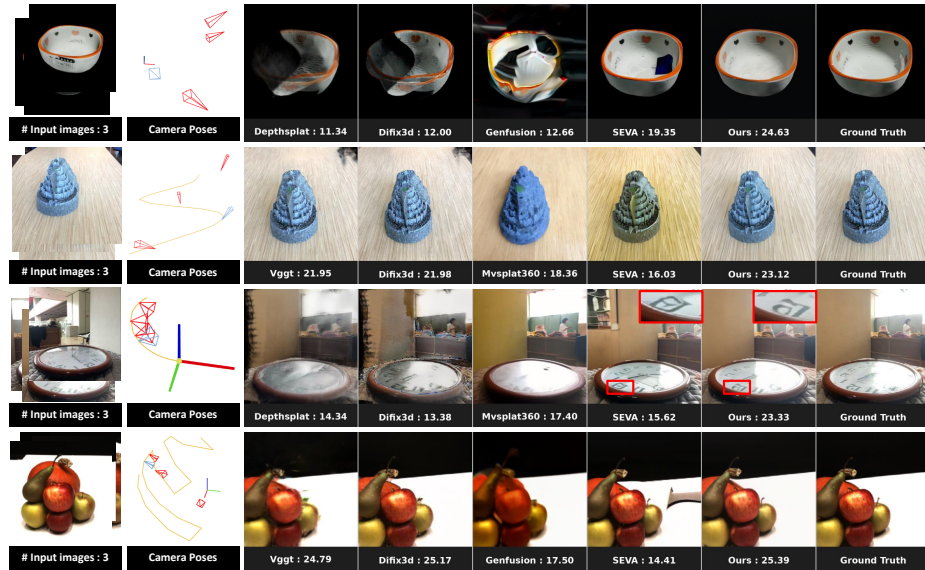


(b) Qualitative results. Given sparse **reference-view** images, novel-view images are synthesized at **target viewpoints**.

Fig. 15 Qualitative results of small-viewpoint NVS.

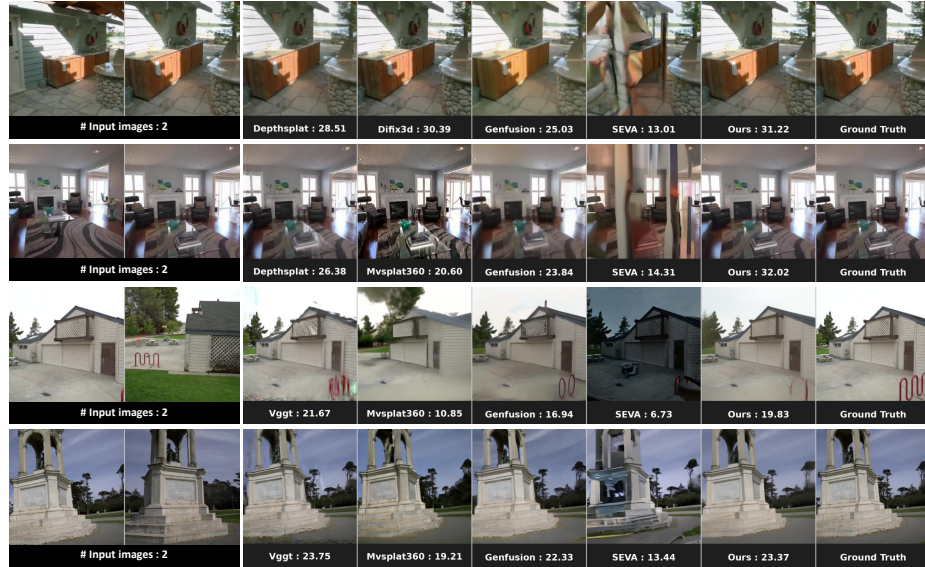


(a) Qualitative results. Given sparse reference-view images, novel-view images are synthesized at target viewpoints.

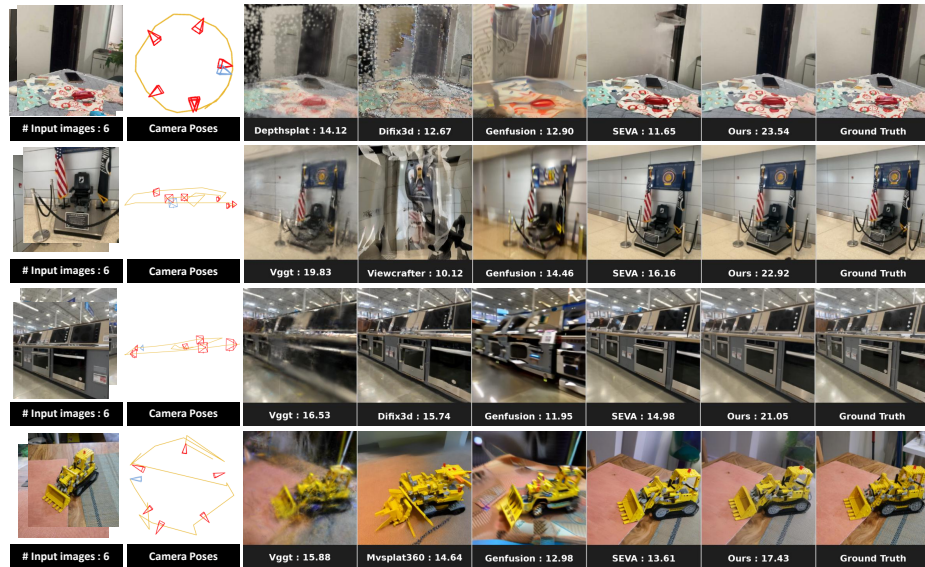


(b) Qualitative results. Given sparse reference-view images, novel-view images are synthesized at target viewpoints.

Fig. 16 Qualitative results of small-viewpoint NVS.

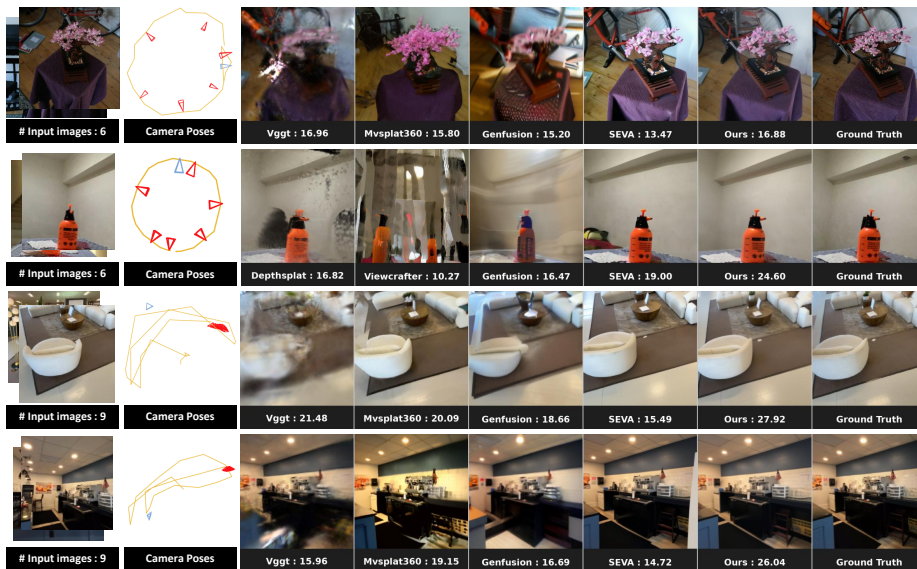


(a) Qualitative results. Given sparse **reference-view** images, novel-view images are synthesized at **target viewpoints**.

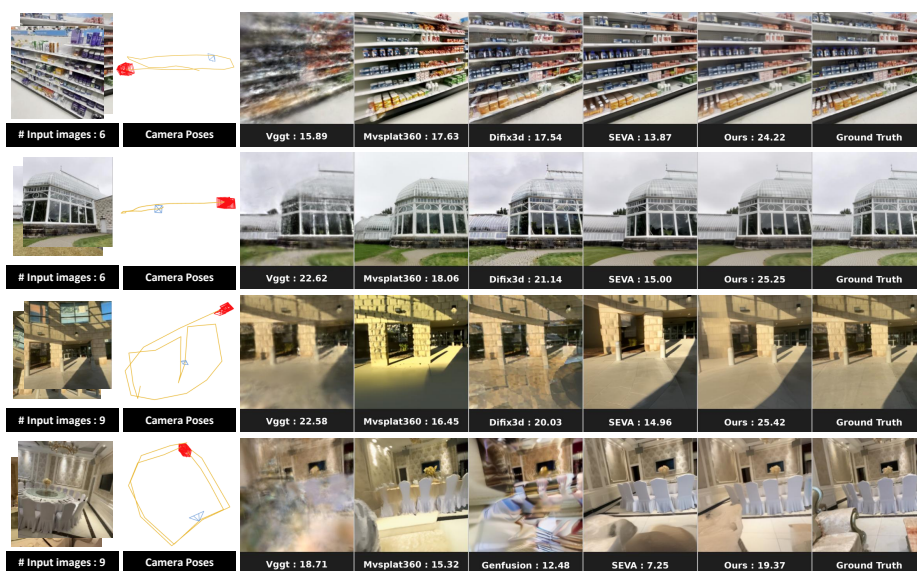


(b) Qualitative results. Given sparse **reference-view** images, novel-view images are synthesized at **target viewpoints**.

Fig. 17 Qualitative results of small-viewpoint NVS.

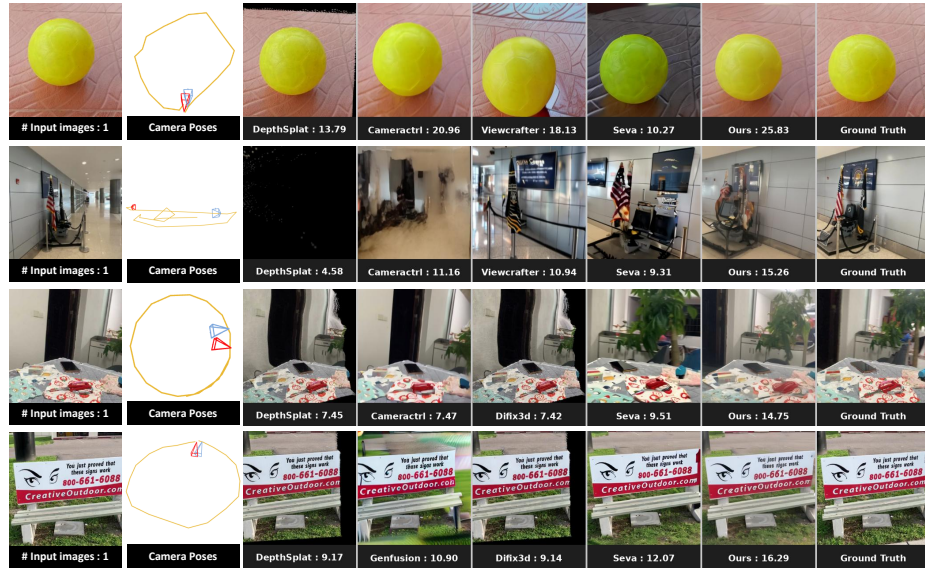


(a) Qualitative results. Given sparse reference-view images, novel-view images are synthesized at target viewpoints.

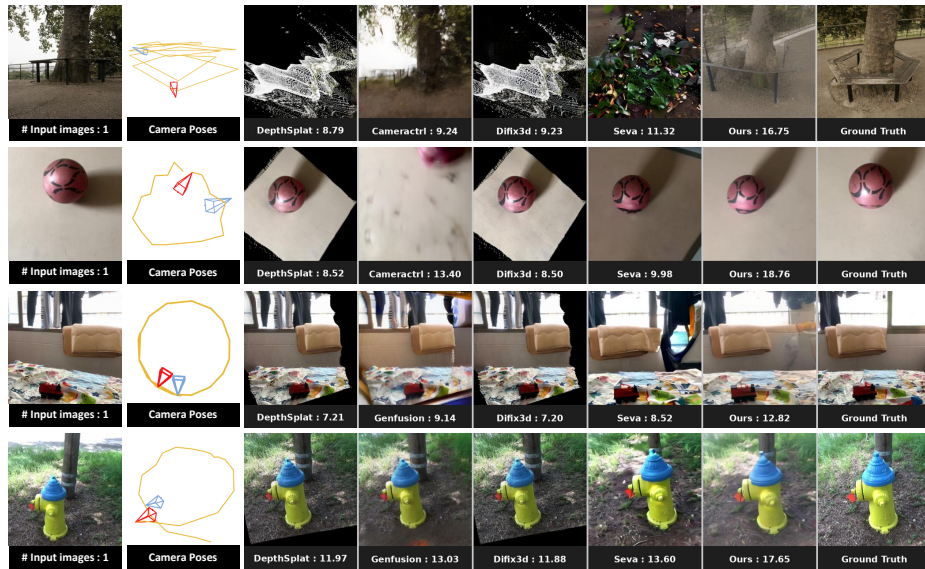


(b) Qualitative results. Given sparse reference-view images, novel-view images are synthesized at target viewpoints.

Fig. 18 Qualitative results of small-viewpoint NVS.

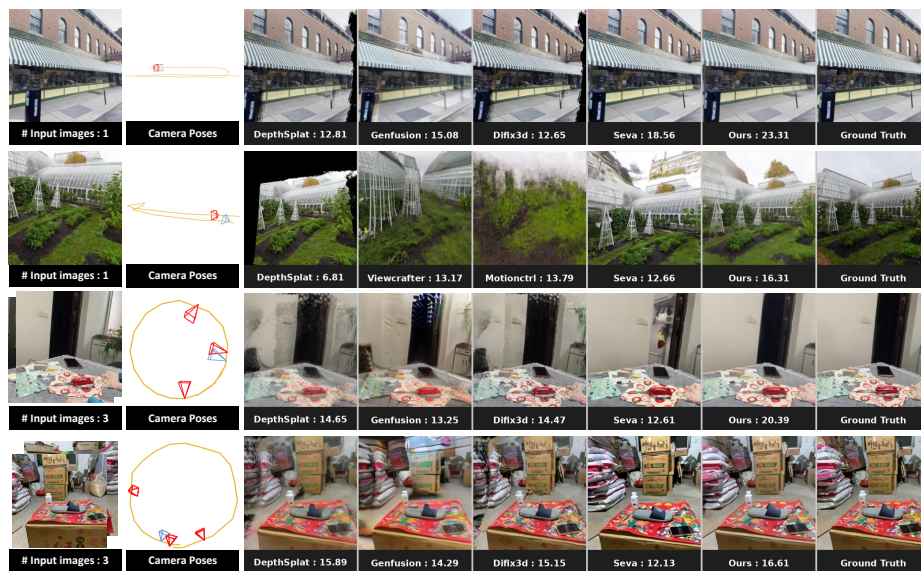


(a) Qualitative results. Given sparse reference-view images, novel-view images are synthesized at target viewpoints.

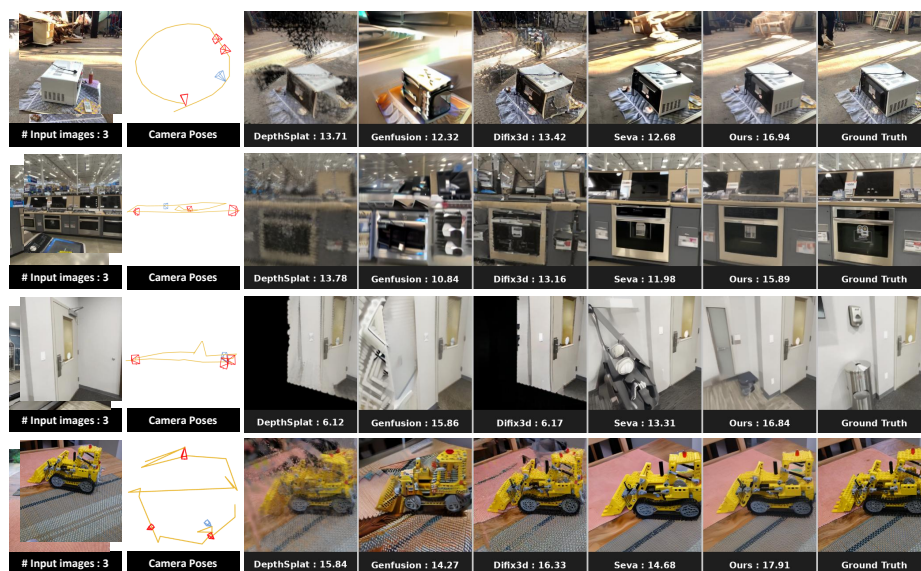


(b) Qualitative results. Given sparse reference-view images, novel-view images are synthesized at target viewpoints.

Fig. 19 Qualitative results of large-viewpoint NVS.

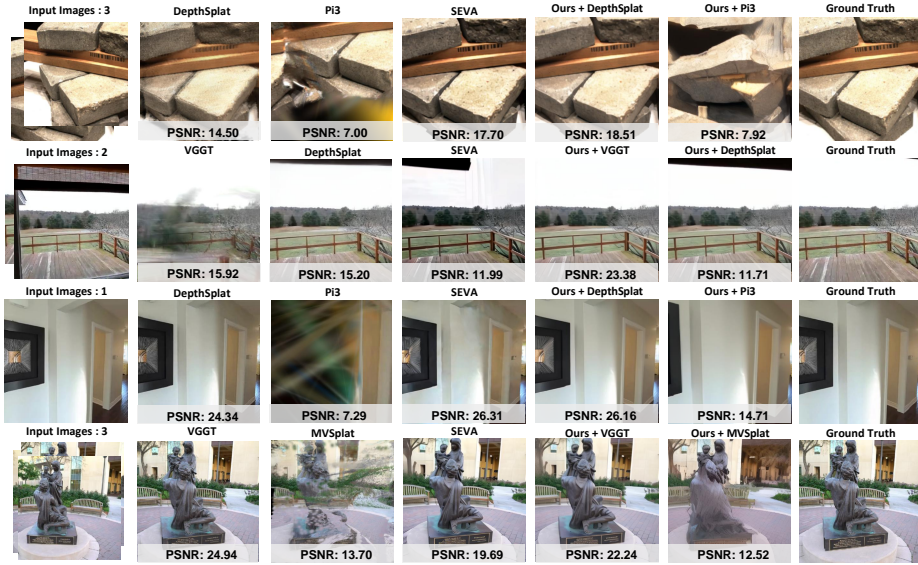


(a) Qualitative results. Given sparse **reference-view** images, novel-view images are synthesized at **target viewpoints**.

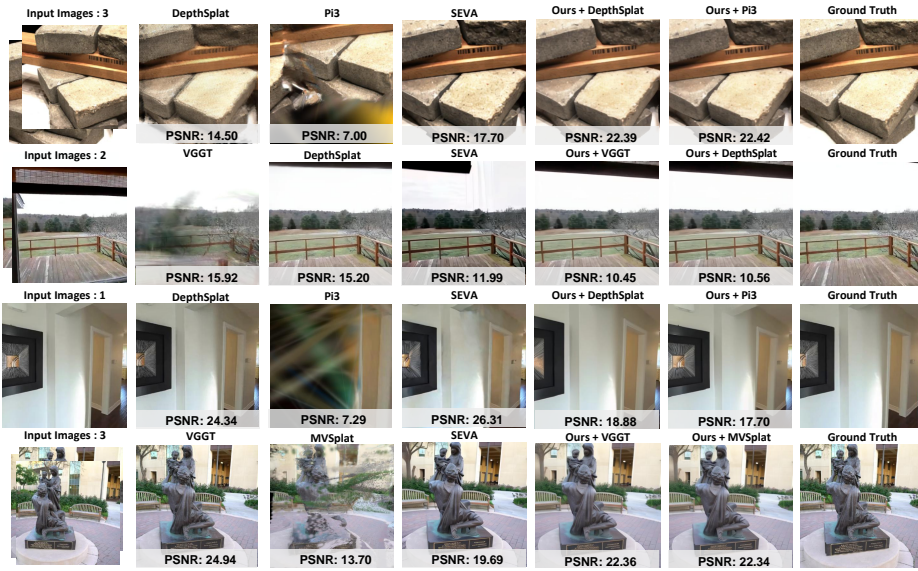


(b) Qualitative results. Given sparse **reference-view** images, novel-view images are synthesized at **target viewpoints**.

Fig. 20 Qualitative results of large-viewpoint NVS.

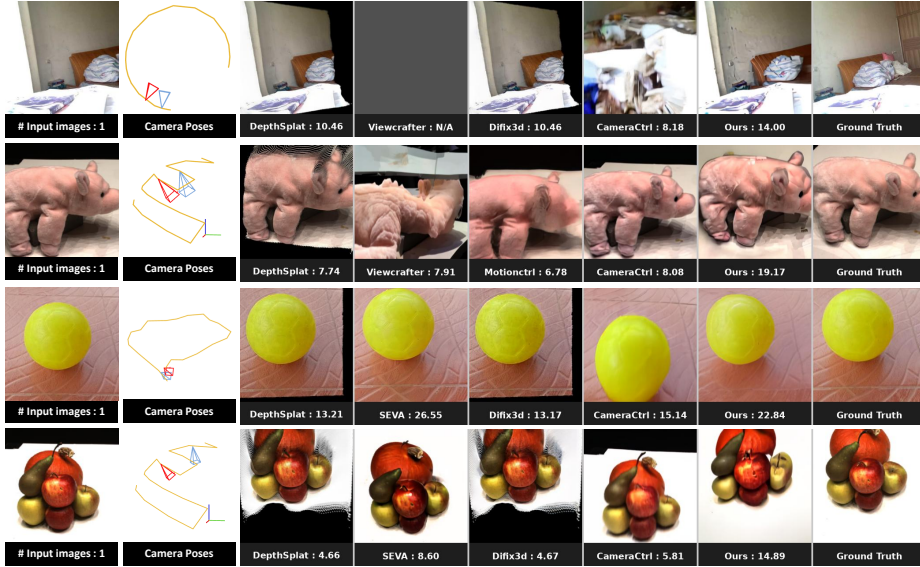


(a) GeoNVS with Naïve Fusion. Naïve fusion heavily relies on the geometry prior quality and fails when the prior is corrupted.

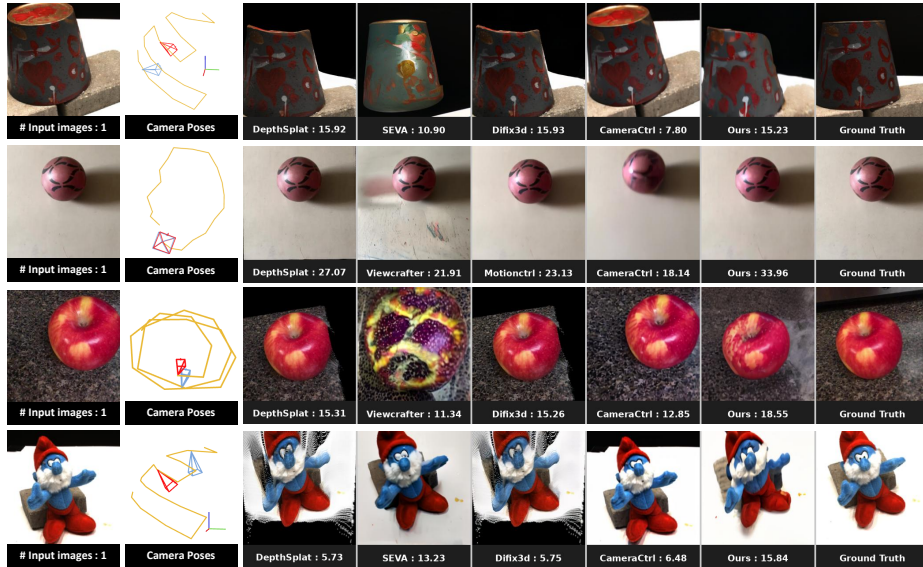


(b) GeoNVS with Adaptive Fusion. Adaptive Fusion substantially mitigates this sensitivity, achieving robust and consistent results regardless of the geometry prior quality.

Fig. 21 Ablation results with various geometry prior in Tab. 5.

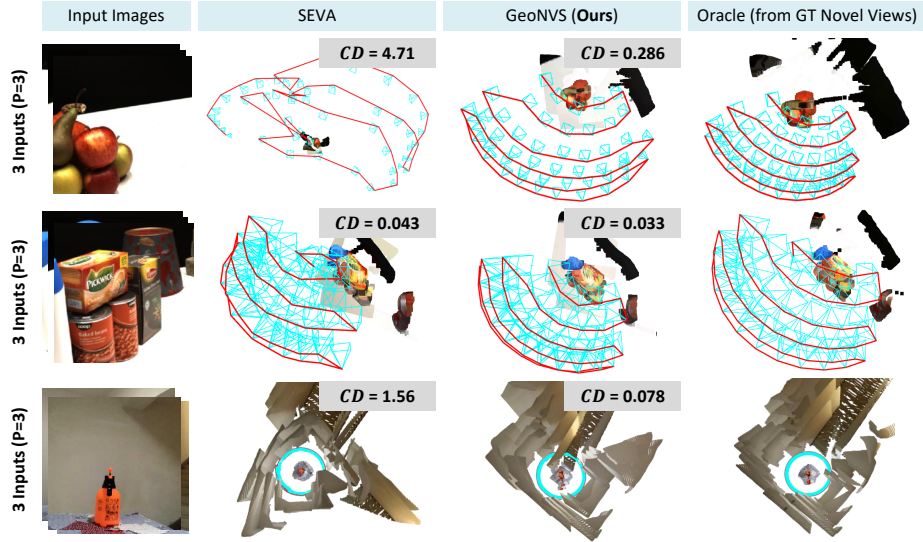


(a) GeoNVS with CameraCtrl [24]. Given sparse reference-view images, novel-view images are synthesized at target viewpoints.

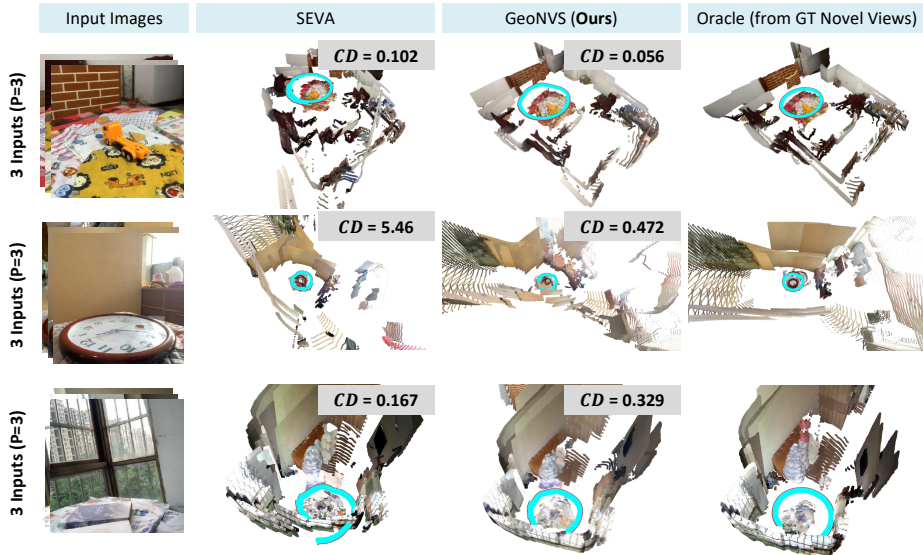


(b) GeoNVS with CameraCtrl [24]. Given sparse reference-view images, novel-view images are synthesized at target viewpoints.

Fig. 22 Ablation results of GeoNVS with CameraCtrl in Tab. 6.



(a) Qualitative results of GeoNVS. 3D reconstruction and camera trajectory estimated from the generated video, showing the improved geometric fidelity of GeoNVS.

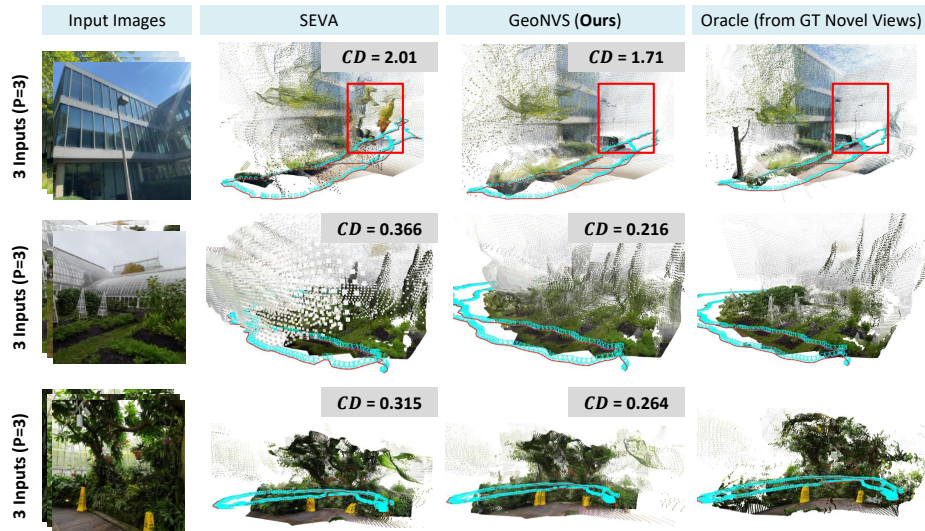


(b) Qualitative results of GeoNVS. 3D reconstruction and camera trajectory estimated from the generated video, showing the improved geometric fidelity of GeoNVS.

Fig. 23 Qualitative results of trajectory NVS.

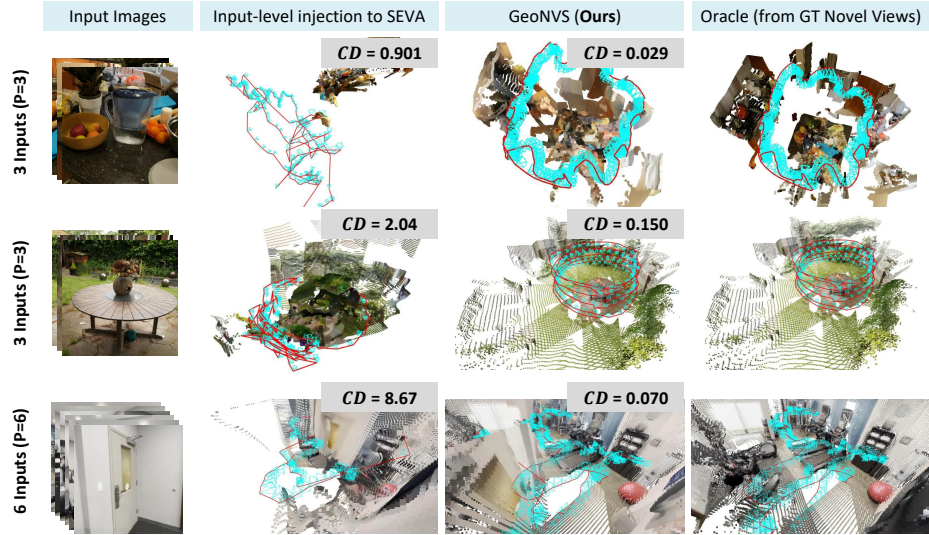


(a) Qualitative results of GeoNVS. 3D reconstruction and camera trajectory estimated from the generated video, showing the improved geometric fidelity of GeoNVS.

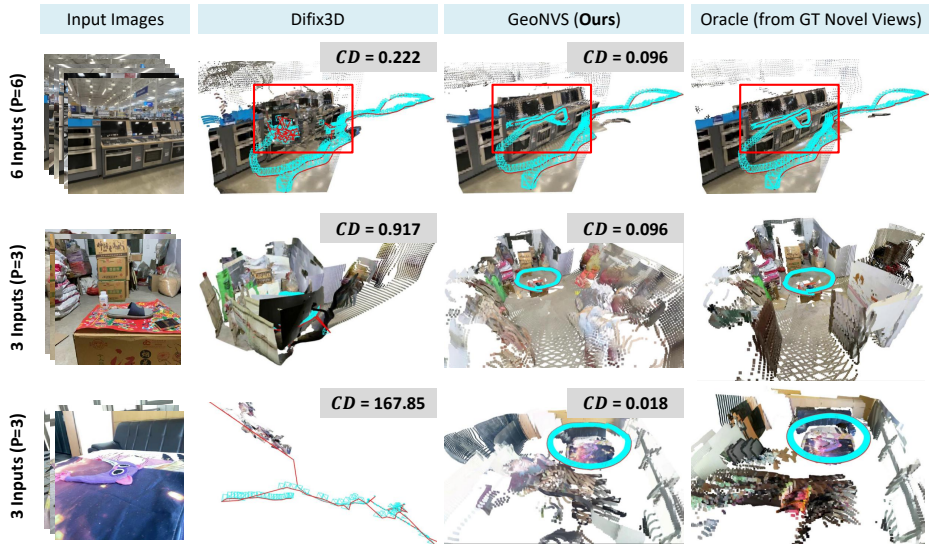


(b) Qualitative results of GeoNVS. 3D reconstruction and camera trajectory estimated from the generated video, showing the improved geometric fidelity of GeoNVS.

Fig. 24 Qualitative results of trajectory NVS.



(a) GeoNVS compared to input-level injection. 3D reconstruction and camera trajectory estimated from the generated video.



(b) GeoNVS compared to difix3d [74]. 3D reconstruction and camera trajectory estimated from the generated video.

Fig. 25 Qualitative results compared to input-level methods in Tab. 4.

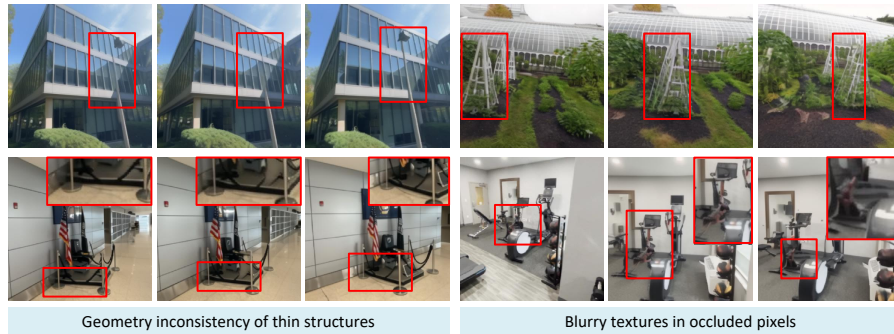


**Fig. 26 Limitations and Failure Cases of GeoNVS.** GeoNVS exhibits geometry inconsistency in thin structures (*left*), where sparse Gaussian representations struggle to capture fine-grained geometry, and blurry textures in occluded regions (*right*), where the geometry prior provides insufficient guidance for unobserved areas.

## References

1. Bai, J., Xia, M., Fu, X., Wang, X., Mu, L., Cao, J., Liu, Z., Hu, H., Bai, X., Wan, P., et al.: Recammaster: Camera-controlled generative rendering from a single video. In: ICCV. pp. 14834–14844 (2025)
2. Barron, J.T., Mildenhall, B., Verbin, D., Srinivasan, P.P., Hedman, P.: Mip-nerf 360: Unbounded anti-aliased neural radiance fields. In: CVPR. pp. 5470–5479 (2022)
3. Blattmann, A., Dockhorn, T., Kulal, S., Mendeleevitch, D., Kilian, M., Lorenz, D., Levi, Y., English, Z., Voleti, V., Letts, A., et al.: Stable video diffusion: Scaling latent video diffusion models to large datasets. arXiv preprint arXiv:2311.15127 (2023)
4. Cao, C., Yu, C., Liu, S., Wang, F., Xue, X., Fu, Y.: Mvgenmaster: Scaling multi-view generation from any image via 3d priors enhanced diffusion model. In: CVPR. pp. 6045–6056 (2025)
5. Caron, M., Touvron, H., Misra, I., Jégou, H., Mairal, J., Bojanowski, P., Joulin, A.: Emerging properties in self-supervised vision transformers. In: ICCV. pp. 9650–9660 (2021)
6. Chan, E.R., Nagano, K., Chan, M.A., Bergman, A.W., Park, J.J., Levy, A., Aittala, M., De Mello, S., Karras, T., Wetzstein, G.: Generative novel view synthesis with 3d-aware diffusion models. In: ICCV. pp. 4217–4229 (2023)
7. Charatan, D., Li, S., Tagliasacchi, A., Sitzmann, V.: pixelsplat: 3d gaussian splats from image pairs for scalable generalizable 3d reconstruction. In: CVPR (2024)
8. Charatan, D., Li, S.L., Tagliasacchi, A., Sitzmann, V.: pixelsplat: 3d gaussian splats from image pairs for scalable generalizable 3d reconstruction. In: CVPR. pp. 19457–19467 (2024)
9. Chen, L.C., Papandreou, G., Kokkinos, I., Murphy, K., Yuille, A.L.: Deeplab: Semantic image segmentation with deep convolutional nets, atrous convolution, and fully connected crfs. *IEEE transactions on pattern analysis and machine intelligence* **40**(4), 834–848 (2017)
10. Chen, Y., Xu, H., Zheng, C., Zhuang, B., Pollefeys, M., Geiger, A., Cham, T.J., Cai, J.: Mvsplat: Efficient 3d gaussian splatting from sparse multi-view images. In: ECCV. pp. 370–386. Springer (2024)
11. Chen, Y., Zheng, C., Xu, H., Zhuang, B., Vedaldi, A., Cham, T.J., Cai, J.: Mvsplat360: Feed-forward 360 scene synthesis from sparse views. In: NeurIPS (2024)
12. Chung, J., Oh, J., Lee, K.M.: Depth-regularized optimization for 3d gaussian splatting in few-shot images. In: CVPR. pp. 811–820 (2024)
13. Deng, K., Liu, A., Zhu, J.Y., Ramanan, D.: Depth-supervised nerf: Fewer views and faster training for free. In: CVPR. pp. 12882–12891 (2022)
14. Duzceker, A., Galliani, S., Vogel, C., Speciale, P., Dusmanu, M., Pollefeys, M.: Deepvideomvs: Multi-view stereo on video with recurrent spatio-temporal fusion. In: CVPR. pp. 15324–15333 (2021)
15. Eftekhari, A., Sax, A., Malik, J., Zamir, A.: Omnidata: A scalable pipeline for making multi-task mid-level vision datasets from 3d scans. In: ICCV. pp. 10786–10796 (2021)
16. Fan, H., Su, H., Guibas, L.J.: A point set generation network for 3d object reconstruction from a single image. In: CVPR. pp. 605–613 (2017)
17. Fan, Z., Wen, K., Cong, W., Wang, K., Zhang, J., Ding, X., Xu, D., Ivanovic, B., Pavone, M., Pavlakos, G., et al.: Instant-splat: Sparse-view gaussian splatting in seconds. arXiv preprint arXiv:2403.20309 (2024)
18. Fu, Y., Liu, S., Kulkarni, A., Kautz, J., Efros, A.A., Wang, X.: Colmap-free 3d gaussian splatting. In: CVPR. pp. 20796–20805 (2024)

19. Gao\*, R., Holynski\*, A., Henzler, P., Brussee, A., Martin-Brualla, R., Srinivasan, P.P., Barron, J.T., Poole\*, B.: Cat3d: Create anything in 3d with multi-view diffusion models. *NeurIPS* (2024)
20. Geng, D., Herrmann, C., Hur, J., Cole, F., Zhang, S., Pfaff, T., Lopez-Guevara, T., Aytar, Y., Rubinstein, M., Sun, C., et al.: Motion prompting: Controlling video generation with motion trajectories. In: *CVPR*. pp. 1–12 (2025)
21. Gu, X., Fan, Z., Zhu, S., Dai, Z., Tan, F., Tan, P.: Cascade cost volume for high-resolution multi-view stereo and stereo matching. In: *CVPR*. pp. 2495–2504 (2020)
22. Gu, Z., Yan, R., Lu, J., Li, P., Dou, Z., Si, C., Dong, Z., Liu, Q., Lin, C., Liu, Z., et al.: Diffusion as shader: 3d-aware video diffusion for versatile video generation control. In: *Proceedings of the Special Interest Group on Computer Graphics and Interactive Techniques Conference Conference Papers*. pp. 1–12 (2025)
23. Hanson, A., Tu, A., Singla, V., Jayawardhana, M., Zwicker, M., Goldstein, T.: Pup 3d-gs: Principled uncertainty pruning for 3d gaussian splatting. In: *CVPR*. pp. 5949–5958 (2025)
24. He, H., Xu, Y., Guo, Y., Wetzstein, G., Dai, B., Li, H., Yang, C.: Cameractrl: Enabling camera control for video diffusion models. In: *ICLR* (2025)
25. He, H., Yang, C., Lin, S., Xu, Y., Wei, M., Gui, L., Zhao, Q., Wetzstein, G., Jiang, L., Li, H.: Cameractrl ii: Dynamic scene exploration via camera-controlled video diffusion models. *arXiv preprint arXiv:2503.10592* (2025)
26. Hu, E.J., Shen, Y., Wallis, P., Allen-Zhu, Z., Li, Y., Wang, S., Wang, L., Chen, W., et al.: Lora: Low-rank adaptation of large language models. *ICLR* **1**(2), 3 (2022)
27. Huang, J., Zhou, Q., Rabeti, H., Korovko, A., Ling, H., Ren, X., Shen, T., Gao, J., Slepichev, D., Lin, C.H., et al.: Vipe: Video pose engine for 3d geometric perception. *arXiv preprint arXiv:2508.10934* (2025)
28. Huang, S.Y., Choe, J., Wang, Y.C.F., Sun, C.: Openvoxel: Training-free grouping and captioning voxels for open-vocabulary 3d scene understanding. *arXiv preprint arXiv:2601.09575* (2026)
29. Im, S., Jeon, H.G., Lin, S., Kweon, I.S.: Dpsnet: End-to-end deep plane sweep stereo. *arXiv preprint arXiv:1905.00538* (2019)
30. Jensen, R., Dahl, A., Vogiatzis, G., Tola, E., Aanaes, H.: Large scale multi-view stereopsis evaluation. In: *CVPR*. pp. 406–413. *IEEE* (2014)
31. Ji, M., Qiu, R.Z., Zou, X., Wang, X.: Grasp splats: Efficient manipulation with 3d feature splatting. *arXiv preprint arXiv:2409.02084* (2024)
32. Jiang, L., Mao, Y., Xu, L., Lu, T., Ren, K., Jin, Y., Xu, X., Yu, M., Pang, J., Zhao, F., et al.: Anysplat: Feed-forward 3d gaussian splatting from unconstrained views. *arXiv preprint arXiv:2505.23716* (2025)
33. Jun-Seong, K., GeonU, K., Yu-Ji, K., Wang, Y.C.F., Choe, J., Oh, T.H.: Dr. splat: Directly referring 3d gaussian splatting via direct language embedding registration. In: *CVPR* (2025)
34. Keetha, N., Müller, N., Schönberger, J., Porzi, L., Zhang, Y., Fischer, T., Knapitsch, A., Zauss, D., Weber, E., Antunes, N., Luiten, J., Lopez-Antequera, M., Bulò, S.R., Richardt, C., Ramanan, D., Scherer, S., Kotschieder, P.: MapAnything: Universal feed-forward metric 3D reconstruction. In: *International Conference on 3D Vision (3DV)*. *IEEE* (2026)
35. Kerbl, B., Kopanas, G., Leimkühler, T., Drettakis, G.: 3d gaussian splatting for real-time radiance field rendering. *ACM Transactions on Graphics* **42**(4) (July 2023), <https://repo-sam.inria.fr/fungraph/3d-gaussian-splatting/>
36. Kerr, J., Kim, C.M., Goldberg, K., Kanazawa, A., Tancik, M.: Lerf: Language embedded radiance fields. In: *ICCV*. pp. 19729–19739 (2023)
37. Kirillov, A., Mintun, E., Ravi, N., Mao, H., Rolland, C., Gustafson, L., Xiao, T., Whitehead, S., Berg, A.C., Lo, W.Y., et al.: Segment anything. In: *ICCV*. pp. 4015–4026 (2023)

38. Knapitsch, A., Park, J., Zhou, Q.Y., Koltun, V.: Tanks and temples: Benchmarking large-scale scene reconstruction. *ACM Transactions on Graphics* **36**(4) (2017)
39. Lee, J., Park, C., Choe, J., Wang, Y.C.F., Kautz, J., Cho, M., Choy, C.: Mosaic3d: Foundation dataset and model for open-vocabulary 3d segmentation. In: *CVPR*. pp. 14089–14101 (2025)
40. Li, L., Zhang, Z., Li, Y., Xu, J., Hu, W., Li, X., Cheng, W., Gu, J., Xue, T., Shan, Y.: Nvcomposer: Boosting generative novel view synthesis with multiple sparse and unposed images. In: *CVPR*. pp. 777–787 (2025)
41. Li, M., Yang, T., Kuang, H., Wu, J., Wang, Z., Xiao, X., Chen, C.: Controlnet++: Improving conditional controls with efficient consistency feedback: Project page: liming-ai.github.io/controlnet\_plus\_plus. In: *ECCV*. pp. 129–147. Springer (2024)
42. Li, W., Zhao, Y., Qin, M., Liu, Y., Cai, Y., Gan, C., Pfister, H.: Langsplatv2: High-dimensional 3d language gaussian splatting with 450+ fps. *Advances in Neural Information Processing Systems* (2025), <https://arxiv.org/abs/2507.07136>
43. Liang, S., Wang, S., Li, K., Niemeyer, M., Gasperini, S., Lensch, H., Navab, N., Tombari, F.: Supergseg: Open-vocabulary 3d segmentation with structured super-gaussians. *arXiv preprint arXiv:2412.10231* (2024)
44. Lin, H., Chen, S., Liew, J., Chen, D.Y., Li, Z., Shi, G., Feng, J., Kang, B.: Depth anything 3: Recovering the visual space from any views. *arXiv preprint arXiv:2511.10647* (2025)
45. Lin, T.Y., Dollár, P., Girshick, R., He, K., Hariharan, B., Belongie, S.: Feature pyramid networks for object detection. In: *CVPR*. pp. 2117–2125 (2017)
46. Ling, L., Sheng, Y., Tu, Z., Zhao, W., Xin, C., Wan, K., Yu, L., Guo, Q., Yu, Z., Lu, Y., et al.: D13dv-10k: A large-scale scene dataset for deep learning-based 3d vision. In: *CVPR*. pp. 22160–22169 (2024)
47. Liu, D., Li, S., Liu, Y., Li, Z., Wang, K., Li, X., Qin, Q., Liu, Y., Xin, Y., Li, Z., et al.: Lumina-video: Efficient and flexible video generation with multi-scale next-dit. *arXiv preprint arXiv:2502.06782* (2025)
48. Liu, X., Zhou, C., Huang, S.: 3dgs-enhancer: Enhancing unbounded 3d gaussian splatting with view-consistent 2d diffusion priors. *NeurIPS* **37**, 133305–133327 (2024)
49. Marrie, J., Ménégau, R., Arbel, M., Larlus, D., Mairal, J.: Ludvig: Learning-free uplifting of 2d visual features to gaussian splatting scenes. In: *ICCV*. pp. 7440–7450 (2025)
50. Meng, C., He, Y., Song, Y., Song, J., Wu, J., Zhu, J.Y., Ermon, S.: Sdedit: Guided image synthesis and editing with stochastic differential equations. *arXiv preprint arXiv:2108.01073* (2021)
51. Mildenhall, B., Srinivasan, P.P., Ortiz-Cayon, R., Kalantari, N.K., Ramamoorthi, R., Ng, R., Kar, A.: Local light field fusion: Practical view synthesis with prescriptive sampling guidelines. *ACM Transactions on Graphics (ToG)* **38**(4), 1–14 (2019)
52. Mildenhall, B., Srinivasan, P.P., Tancik, M., Barron, J.T., Ramamoorthi, R., Ng, R.: Nerf: Representing scenes as neural radiance fields for view synthesis. *Communications of the ACM* **65**(1), 99–106 (2021)
53. Oquab, M., Darcet, T., Moutakanni, T., Vo, H., Szafraniec, M., Khalidov, V., Fernandez, P., Haziza, D., Massa, F., El-Nouby, A., et al.: Dinov2: Learning robust visual features without supervision. *arXiv preprint arXiv:2304.07193* (2023)
54. Qin, M., Li, W., Zhou, J., Wang, H., Pfister, H.: Langsplat: 3d language gaussian splatting. In: *CVPR*. pp. 20051–20060 (2024)
55. Radford, A., Kim, J.W., Hallacy, C., Ramesh, A., Goh, G., Agarwal, S., Sastry, G., Askell, A., Mishkin, P., Clark, J., et al.: Learning transferable visual models from natural language supervision. In: *ICML*. pp. 8748–8763. PmLR (2021)

56. Ranftl, R., Bochkovskiy, A., Koltun, V.: Vision transformers for dense prediction. In: ICCV. pp. 12179–12188 (2021)
57. Reizenstein, J., Shapovalov, R., Henzler, P., Sbordone, L., Labatut, P., Novotny, D.: Common objects in 3d: Large-scale learning and evaluation of real-life 3d category reconstruction. In: CVPR. pp. 10901–10911 (2021)
58. Ren, X., Shen, T., Huang, J., Ling, H., Lu, Y., Nimier-David, M., Müller, T., Keller, A., Fidler, S., Gao, J.: Gen3c: 3d-informed world-consistent video generation with precise camera control. In: CVPR. pp. 6121–6132 (2025)
59. Rombach, R., Blattmann, A., Lorenz, D., Esser, P., Ommer, B.: High-resolution image synthesis with latent diffusion models. In: CVPR. pp. 10684–10695 (2022)
60. Schönberger, J.L., Frahm, J.M.: Structure-from-motion revisited. In: CVPR (2016)
61. Schönberger, J.L., Zheng, E., Pollefeys, M., Frahm, J.M.: Pixelwise view selection for unstructured multi-view stereo. In: ECCV (2016)
62. Seo, S., Chang, Y., Kwak, N.: Flipnerf: Flipped reflection rays for few-shot novel view synthesis. In: ICCV. pp. 22883–22893 (2023)
63. Tang, S., Ye, W., Ye, P., Lin, W., Zhou, Y., Chen, T., Ouyang, W.: Hisplat: Hierarchical 3d gaussian splatting for generalizable sparse-view reconstruction. In: ICLR (2025)
64. Wang, G., Chen, Z., Loy, C.C., Liu, Z.: Sparsenerf: Distilling depth ranking for few-shot novel view synthesis. In: ICCV. pp. 9065–9076 (2023)
65. Wang, J., Chen, M., Karaev, N., Vedaldi, A., Rupprecht, C., Novotny, D.: Vggt: Visual geometry grounded transformer. In: CVPR. pp. 5294–5306 (2025)
66. Wang, J., Sun, K., Cheng, T., Jiang, B., Deng, C., Zhao, Y., Liu, D., Mu, Y., Tan, M., Wang, X., et al.: Deep high-resolution representation learning for visual recognition. IEEE transactions on pattern analysis and machine intelligence **43**(10), 3349–3364 (2020)
67. Wang, S., Zhang, S., Millerdurai, C., Westermann, R., Stricker, D., Pagani, A.: Inpaint360gs: Efficient object-aware 3d inpainting via gaussian splatting for 360 {deg} scenes. arXiv preprint arXiv:2511.06457 (2025)
68. Wang, S., Leroy, V., Cabon, Y., Chidlovskii, B., Revaud, J.: Dust3r: Geometric 3d vision made easy. In: CVPR. pp. 20697–20709 (2024)
69. Wang, W., Xie, E., Li, X., Fan, D.P., Song, K., Liang, D., Lu, T., Luo, P., Shao, L.: Pyramid vision transformer: A versatile backbone for dense prediction without convolutions. In: ICCV. pp. 568–578 (2021)
70. Wang, Y., Zhou, J., Zhu, H., Chang, W., Zhou, Y., Li, Z., Chen, J., Pang, J., Shen, C., He, T.:  $\pi^3$ : Scalable permutation-equivariant visual geometry learning (2025), <https://arxiv.org/abs/2507.13347>
71. Wang, Z., Yuan, Z., Wang, X., Li, Y., Chen, T., Xia, M., Luo, P., Shan, Y.: Motionctrl: A unified and flexible motion controller for video generation. In: SIGGRAPH. pp. 1–11 (2024)
72. Watson, D., Saxena, S., Li, L., Tagliasacchi, A., Fleet, D.J.: Controlling space and time with diffusion models. arXiv preprint arXiv:2407.07860 (2024)
73. Wu, H., Wu, D., He, T., Guo, J., Ye, Y., Duan, Y., Bian, J.: Geometry forcing: Marrying video diffusion and 3d representation for consistent world modeling. arXiv preprint arXiv:2507.07982 (2025)
74. Wu, J.Z., Zhang, Y., Turki, H., Ren, X., Gao, J., Shou, M.Z., Fidler, S., Gojcic, Z., Ling, H.: Difix3d+: Improving 3d reconstructions with single-step diffusion models. In: CVPR. pp. 26024–26035 (2025)
75. Wu, R., Mildenhall, B., Henzler, P., Park, K., Gao, R., Watson, D., Srinivasan, P.P., Verbin, D., Barron, J.T., Poole, B., et al.: Reconfusion: 3d reconstruction with diffusion priors. In: CVPR. pp. 21551–21561 (2024)

76. Wu, S., Xu, C., Huang, B., Geiger, A., Chen, A.: Genfusion: Closing the loop between reconstruction and generation via videos. In: CVPR. pp. 6078–6088 (2025)
77. Wu, T., Zhang, J., Fu, X., Wang, Y., Ren, J., Pan, L., Wu, W., Yang, L., Wang, J., Qian, C., et al.: Omniobject3d: Large-vocabulary 3d object dataset for realistic perception, reconstruction and generation. In: CVPR. pp. 803–814 (2023)
78. Wu, W., Li, Z., Gu, Y., Zhao, R., He, Y., Zhang, D.J., Shou, M.Z., Li, Y., Gao, T., Zhang, D.: Draganything: Motion control for anything using entity representation. In: ECCV. pp. 331–348. Springer (2024)
79. Xia, H., Fu, Y., Liu, S., Wang, X.: Rgb-d objects in the wild: Scaling real-world 3d object learning from rgb-d videos. In: CVPR. pp. 22378–22389 (2024)
80. Xu, H., Peng, S., Wang, F., Blum, H., Barath, D., Geiger, A., Pollefeys, M.: Depth-splat: Connecting gaussian splatting and depth. In: CVPR. pp. 16453–16463 (2025)
81. Yang, L., Kang, B., Huang, Z., Xu, X., Feng, J., Zhao, H.: Depth anything: Unleashing the power of large-scale unlabeled data. In: CVPR. pp. 10371–10381 (2024)
82. Yao, Y., Luo, Z., Li, S., Fang, T., Quan, L.: Mvsnet: Depth inference for unstructured multi-view stereo. ECCV (2018)
83. Yin, S., Wu, C., Liang, J., Shi, J., Li, H., Ming, G., Duan, N.: Dragnuwa: Fine-grained control in video generation by integrating text, image, and trajectory. arXiv preprint arXiv:2308.08089 (2023)
84. Yin, W., Zhang, C., Chen, H., Cai, Z., Yu, G., Wang, K., Chen, X., Shen, C.: Metric3d: Towards zero-shot metric 3d prediction from a single image. In: CVPR. pp. 9043–9053 (2023)
85. Yin, X., Zhang, Q., Chang, J., Feng, Y., Fan, Q., Yang, X., Pun, C.M., Zhang, H., Cun, X.: Gsfixer: Improving 3d gaussian splatting with reference-guided video diffusion priors. arXiv preprint arXiv:2508.09667 (2025)
86. Yu, W., Xing, J., Yuan, L., Hu, W., Li, X., Huang, Z., Gao, X., Wong, T.T., Shan, Y., Tian, Y.: Viewcrafter: Taming video diffusion models for high-fidelity novel view synthesis. arXiv preprint arXiv:2409.02048 (2024)
87. Yu, Z., Peng, S., Niemeyer, M., Sattler, T., Geiger, A.: Monosdf: Exploring monocular geometric cues for neural implicit surface reconstruction. NeurIPS **35**, 25018–25032 (2022)
88. Zhang, L., Rao, A., Agrawala, M.: Adding conditional control to text-to-image diffusion models. In: ICCV. pp. 3836–3847 (2023)
89. Zhang, Z., Liao, J., Li, M., Dai, Z., Qiu, B., Zhu, S., Qin, L., Wang, W.: Tora: Trajectory-oriented diffusion transformer for video generation. In: CVPR. pp. 2063–2073 (2025)
90. Zhou, J., Gao, H., Voleti, V., Vasishtha, A., Yao, C.H., Boss, M., Torr, P., Rupprecht, C., Jampani, V.: Stable virtual camera: Generative view synthesis with diffusion models. arXiv preprint arXiv:2503.14489 (2025)
91. Zhou, S., Chang, H., Jiang, S., Fan, Z., Zhu, Z., Xu, D., Chari, P., You, S., Wang, Z., Kadambi, A.: Feature 3dgs: Supercharging 3d gaussian splatting to enable distilled feature fields. In: CVPR. pp. 21676–21685 (2024)
92. Zhou, T., Tucker, R., Flynn, J., Fyffe, G., Snavely, N.: Stereo magnification: Learning view synthesis using multiplane images. arXiv preprint arXiv:1805.09817 (2018)
93. Zhu, Z., Fan, Z., Jiang, Y., Wang, Z.: Fsgs: Real-time few-shot view synthesis using gaussian splatting. In: ECCV. pp. 145–163. Springer (2024)
94. Ziwen, C., Tan, H., Zhang, K., Bi, S., Luan, F., Hong, Y., Fuxin, L., Xu, Z.: Long-irm: Long-sequence large reconstruction model for wide-coverage gaussian splats. arXiv preprint 2410.12781 (2024)